nature communications

Article

https://doi.org/10.1038/s41467-024-55223-9

Aptamer-conjugated gold nanoparticles enable oligonucleotide delivery into muscle stem cells to promote regeneration of dystrophic muscles

Received: 1 February 2024

Accepted: 3 December 2024

Francesco Millozzi[1,2,11], **Paula Milán-Rois**[3,11], **Arghya Sett**[4,10], **Giovanni Delli Carpini**[1], **Marco De Bardi**[5], **Miguel Gisbert-Garzarán**[3], **Martina Sandonà**[1,5], **Ciro Rodríguez-Díaz**[3], **Mario Martínez-Mingo**[3], **Irene Pardo**[3], **Federica Esposito**[2,5], **Maria Teresa Viscomi**[1,6], **Marina Bouché**[2], **Ornella Parolini**[1,6], **Valentina Saccone**[1,6], **Jean-Jacques Toulmé**[4,7] ✉, **Álvaro Somoza**[3,8] ✉ & **Daniela Palacios**[1,9] ✉

Inefficient targeting of muscle stem cells (MuSCs), also called satellite cells, represents a major bottleneck of current therapeutic strategies for muscular dystrophies, as it precludes the possibility of promoting compensatory regeneration. Here we describe a muscle-targeting delivery platform, based on gold nanoparticles, that enables the release of therapeutic oligonucleotides into MuSCs. We demonstrate that AuNPs conjugation to an aptamer against α7/β1 integrin dimers directs either local or systemic delivery of microRNA-206 to MuSCs, thereby promoting muscle regeneration and improving muscle functionality, in a mouse model of Duchenne Muscular Dystrophy. We show here that this platform is biocompatible, non-toxic, and non-immunogenic, and it can be easily adapted for the release of a wide range of therapeutic oligonucleotides into diseased muscles.

Duchenne Muscular Dystrophy (DMD; ONIM: #310200) is the most common and severe form of genetic muscular dystrophy, caused by mutations in the dystrophin gene that lead to a complete absence of the protein[1]. In Duchenne patients, the lack of dystrophin results in structural destabilization of the sarcolemma and increased sensitivity to contraction-induced fibre damage. This leads to a progressive loss of muscle mass that is then replaced with fibrotic and adipose tissue[2]. There is currently no cure for the disease, and the standard-of-care treatment aims at palliating the disease symptoms through corticosteroids, breathing aids, and physiotherapy[3,4]. Attempts to recover a functional version of the protein via gene and oligonucleotide-based therapies are in advanced phases of clinical development[5,6]. However, the vast extension of skeletal muscle, which accounts for 30–40% of the body mass, together with the exacerbated muscle damage present in dystrophic patients, poses extra challenges to these approaches.

Current clinical trials of gene therapies have been evaluated by outcome measures that indicate low delivery and expression of micro-

---

[1]Department of Life Science and Public Health, Università Cattolica del Sacro Cuore, Rome, Italy. [2]Department of Anatomical, Histological, Forensic Medicine and Orthopaedic Sciences, Section of Histology and Embryology, Sapienza University of Rome, Rome, Italy. [3]IMDEA Nanociencia, Madrid, Spain. [4]Bordeaux University, Inserm U1212, CNRS UMR5320 Bordeaux, France. [5]Fondazione Santa Lucia IRCCS, Rome, Italy. [6]Fondazione Policlinico, Universitario Agostino Gemelli IRCCS, Rome, Italy. [7]Novaptech, Gradignan, France. [8]Unidad Asociada de Nanobiomedicina, Centro Nacional de Biotecnología (CNB-CSIC), Madrid, Spain. [9]Institute for Systems Analysis and Computer Science "Antonio Ruberti" (IASI), National Research Council (CNR), Rome, Italy. [10]Present address: ERIN Department, Luxembourg Institute of Science and Technology (LIST), Belvaux, Luxembourg. [11]These authors contributed equally: Francesco Millozzi, Paula Milán-Rois. ✉e-mail: jj.toulme@novaptech.com; alvaro.somoza@imdea.org; daniela.palacios@cnr.it

dystrophin, with no evidence of functional improvement, indicating that gene delivery approaches are amenable of improvement. In addition, available technologies show very little evidence of effective delivery to muscle stem cells (MuSCs)[4,5,7], the direct effectors of muscle regeneration. As MuSC ability to regenerate DMD muscles is severely impaired by the loss of dystrophin[8–11] as well as by disease-associated intrinsic[12,13] or extrinsic[14,15] anti-myogenic signals, correction of MuSCs' ability to regenerate DMD muscles represents an imperative task for an effective therapeutic intervention. Yet, the lack of technologies for direct and specific targeting of MuSCs for the delivery of therapeutic agents has complicated this task and represents a current bottleneck in DMD therapeutics.

Work from the past few years has revealed that paracrine molecules released by muscle fibres or muscle-resident cells can regulate MuSC function and stimulate skeletal muscle regeneration. Of them, microRNAs (miRNAs) have recently emerged as potential therapeutic molecules for DMD and other muscle disorders[16]. MirRNAs are small non-coding RNAs of around 22 nucleotides that regulate gene expression post-transcriptionally. MiRNA binding to the 3′ untranslated region (UTR) of target mRNAs leads to reduced gene expression by either degradation of the target mRNA or translational inhibition[17]. Several muscle-specific miRNAs, the so-called myomirs, are associated with MuSC function and muscle regeneration[18,19]. Myomirs are dynamically regulated and play a fundamental role in regulating muscle lineage determination[20,21] as well as MuSCs quiescence, activation, and differentiation[20,22,23]. In addition, MuSCs respond not only to endogenously produced miRNAs, but also to miRNAs released by skeletal muscle fibres[24] and non-myogenic resident cells, such as fibro-adipogenic progenitors (FAPs)[25,26]. Altogether, these studies suggest that modulation of miRNA levels in MuSCs may be an effective therapeutic approach to potentiate the regeneration of dystrophic muscles.

Amongst the miRNAs with therapeutic potential for muscle diseases, miR-206 plays important roles both in MuSCs differentiation and in skeletal muscle regeneration. Using knock-out mice, Liu et al. showed that miR-206 promotes skeletal muscle regeneration and delays disease progression in a mouse model of DMD[27]. Under physiological conditions, miR-206 expression is restricted to the skeletal muscle lineage. However, miR-206 is also produced and released within extra-cellular vesicles (EVs) by FAPs, upon treatment of dystrophic mice with histone deacetylases (HDACs) inhibitors[26]. HDAC inhibitors have been shown to promote skeletal muscle regeneration and ameliorate the dystrophic phenotype in pre-clinical models of DMD[28–30], leading to FDA approval of one of such inhibitors, givinostat, for the treatment of DMD patients[31]. Recent studies demonstrated that the pro-regenerative effect of HDAC inhibitors is mediated, at least in part, by FAPs-released EVs containing miR-206, which target MuSCs[25]. Altogether, these works highlight the importance of miR-206 in skeletal muscle regeneration, pointing it out as a potential therapeutic molecule to restore MuSC ability to regenerate DMD muscles.

However, as occurs with other oligonucleotide-based therapies, in vivo delivery of miRNAs presents several caveats, including poor pharmacokinetic properties and low stability. Several strategies have been employed to increase oligonucleotide stability in the bloodstream and to improve cellular uptake, such as the use of chemical modifications or conjugation to lipids, cell-penetrating peptides and polymers[6]. However, there is still the need to improve the selective delivery of high amounts of therapeutic molecules into skeletal muscle tissue. Within this context, nanotechnologies may provide efficient and safe biocarriers for oligonucleotide-based therapeutics. A variety of nanostructures can be modified with different types of oligonucleotides, such as miRNAs, small interference RNAs (siRNAs), and antisense oligonucleotides (ASOs). Of them, gold nanoparticles (AuNPs) stand out due to their small size, high functionalization capacity, and low toxicity[32–36]. The use of AuNPs densely covered by oligonucleotides, also known as spherical nucleic acids (SNAs), not only improves the stability of nucleic acids in the bloodstream but also increases their cellular uptake. Additionally, AuNPs can also be easily conjugated to different targeting moieties (e.g., antibodies, peptides, and aptamers) to improve tissue selectivity and therefore reduce off-target effects[37].

Here, we developed a delivery platform, based on functionalized AuNPs, to specifically release therapeutic oligonucleotides into skeletal muscles. The platform is composed of a gold core and a dense, packed shell of nucleic acids[38]. This kind of packed distribution prevents oligonucleotide degradation, improving their pharmacokinetics and enhancing the therapeutic effect[39]. To achieve selective muscle targeting, the AuNPs were conjugated to an aptamer against the extracellular portion of α7/β1 integrin dimers, a highly specific surface receptor expressed by muscle progenitors and differentiated myofibers that is virtually absent in other organs or tissues[40,41]. Our data show that aptamer-conjugated AuNPs efficiently target skeletal muscles, including highly inaccessible muscles such as the diaphragm, with a high selectivity towards the MuSCs compartment. Moreover, systemic treatment with miR-206 containing AuNPs increases skeletal muscle regeneration and improves muscle functionality in a mouse model of DMD. Thanks to its versatility, this platform can be implemented to deliver different types of therapeutic molecules, including other types of nucleic acids, small molecules, and proteins[42–44].

Results

Development of a muscle-specific aptamer

To obtain muscle-specific targeting, we developed an aptamer against the extra-cellular portion of the α7/β1 integrin dimer. α7/β1 integrins are enriched in muscle tissues, and are highly expressed in MuSCs, but they are absent in other organs or tissues[40,41]. The aptamer was obtained through Systematic Evolution of Ligands by Exponential Enrichment (SELEX) from a library of 10^{14} DNA sequences. Briefly, cross-over SELEX was performed simultaneously against Histidine-tagged α7/β1 integrin recombinant protein and C2C12 muscle cells (Supplementary Fig. 1a) as described previously[45].

After 14 rounds of selection, the pools eluted from each round and the initial library were submitted to Next Generation Sequencing and sequences were analyzed with bioinformatincs tools (Multiple sequence alignment MAFFT motif analyses, cluster analysis, secondary structure analysis). Following this analysis, 8 potential aptamer candidates were selected, and their binding properties were further investigated by Surface Plasmon Resonance (SPR) (Fig. 1a). The most efficient binder, NM15, with a K_D of about 235 nM was further truncated to eliminate the conserved flanking regions to obtain NM15.2, with a K_D of about 40 nM. The ability of NM15.2 to recognize C2C12 cells was then investigated by cytofluorimetry, using an Alexa-594 5′-end conjugated aptamer. The results shown in Supplementary Fig. 1b demonstrate that over 85% of C2C12 cells were efficiently labelled with NM15.2, confirming its ability to recognize muscle cells.

The specificity of NM15.2 -hereinafter α7/β1 aptamer- towards MuSCs and skeletal muscle fibres was then assessed using Alexa-594 5′ end-labelled oligonucleotides. Flow cytofluorimetry experiments in muscles isolated from dystrophic D2.B10-Dmd^{mdx}/J (D2-mdx) mice using antibodies against CD31, CD45, TER119 and SCA1 and the Alexa-594 5′-end conjugated α7/β1 aptamer confirmed the specificity of the α7/β1 aptamer towards a muscle-resident population defined as negative for both hematopoietic, endothelial and mesenchymal surface markers (CD31, CD45, TER119, SCA1), and likely corresponding to MuSCs. A scramble oligonucleotide of the same length was used as a negative control, showing a much-reduced binding (Supplementary Fig. 1c and Fig. 1b, c). Moreover, confocal microscopy on single myofibres isolated from dystrophic mice confirmed a positive α7/β1 aptamer staining on PAX7-positive MuSCs (Fig. 1d). Finally, staining on transversal sections of Tibialis Anterior (TA) muscles from dystrophic

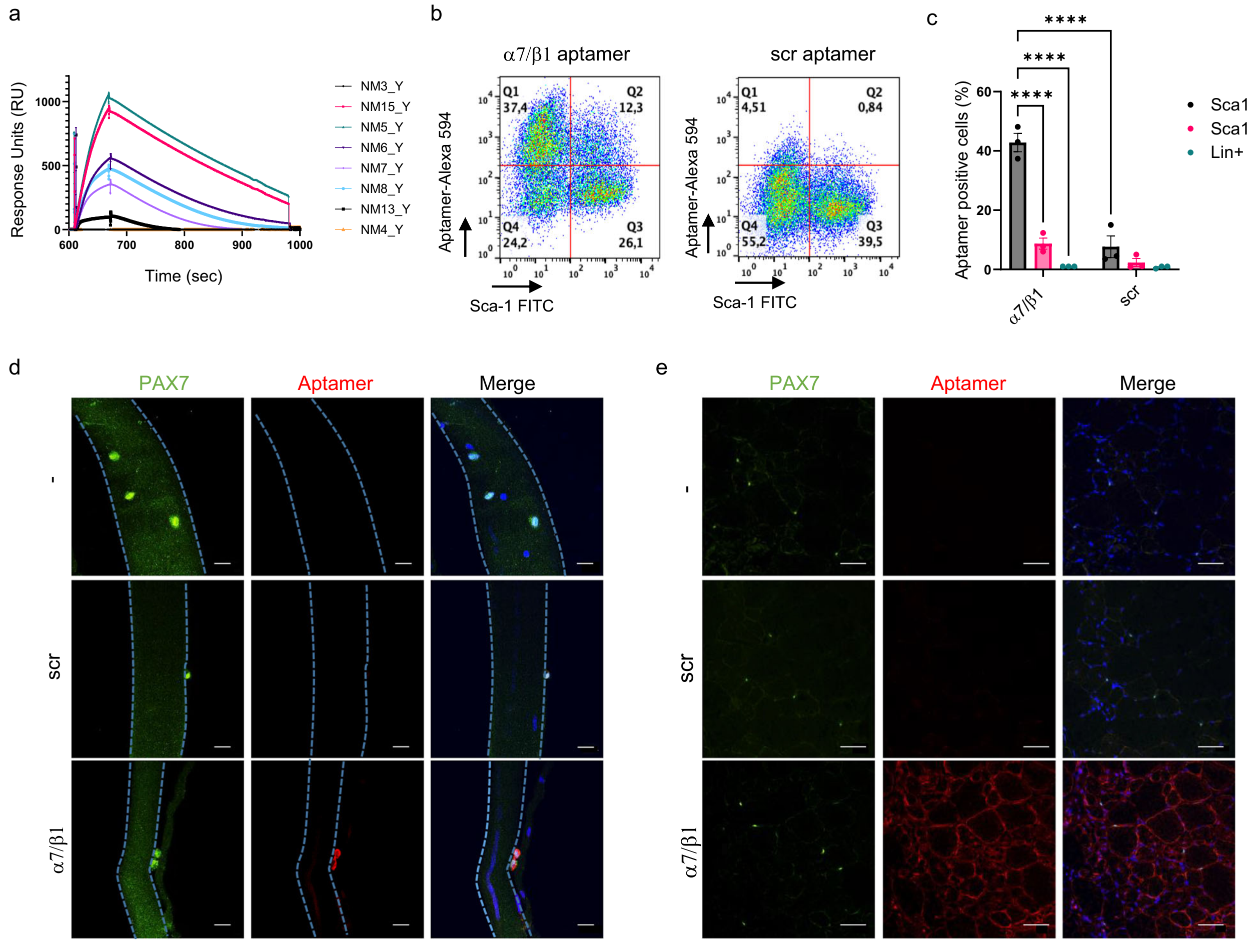

Fig. 1 | Selection and characterization of a muscle-specific aptamer against α7/β1 integrin dimers. a Sensogram obtained by Surface Plasmon Resonance (SPR) for the association with and the dissociation from α7/β1 integrin recombinant protein of selected aptamer candidates. **b** Representative flow cytometry plot showing α7/β1 aptamer-positive cells (y-axis) and Sca1-positive cells (x-axis) on the lineage (CD31, CD45, TER119)-negative muscle resident cells. A scramble (scr) aptamer was included as a negative control. **c** Percentage of α7/β1 aptamer-positive, Sca1-negative cells (grey), α7/β1 aptamer-negative, Sca1-positive cells (pink) and lineage positive (lin +) cells (green) in the gastrocnemius muscles of D2-mdx mice analyzed by flow cytometry in (**b**). Data are presented as mean values +/- SEM (*n* = 3 mice). Statistical analysis was performed using two-way ANOVA followed by Tukey's *post hoc* test. **d** Fluorescence analysis on freshly isolated myofibres using an Alexa 594-labelled α7/β1 aptamer and Alexa 594-scr as a control. The panels show representative images of three independent experiments, with similar results. Scale bar: 20 µm. **e** Fluorescence analysis on transversal sections of Tibialis Anterior (TA) muscles using an Alexa 594- α7/β1 aptamer. Scramble aptamer and un-hybridized sections were included as a negative controls. The panels show representative images from sections of three independent TA muscles. Scale bar: 50 µm.

D2-mdx mice showed that the Alexa-594 5′ end-labelled α7/β1 aptamer is also able to stain muscle fibres membrane, as expected[46,47] (Fig. 1e). Altogether, these results indicate that the α7/β1 aptamer efficiently binds skeletal muscles, including MuSCs and myofibers, in a mouse model of DMD.

Generation of aptamer-conjugated AuNPs for oligonucleotide delivery

We next conjugated either control (scr) or α7/β1 aptamers, together with two different types of cargo oligonucleotides (miR-206 mimics, and oligodT) to the AuNPs as follows. AuNPs were first synthetized through the Turkevich method, yielding spherical nanoparticles with a size of *ca*. 15 nm (Fig. 2a). Then, 5′ end-thiolated aptamers and 3′ end-thiolated cargo oligonucleotides were added to the AuNPs, which were further salt-aged to improve the packing of the nucleic acids. The successful coating was verified by the lack of changes in the absorbance spectrum, showing all of them a maximum at 520 nm, typical of this kind of nanomaterials (Fig. 2b). The colloidal stability of the different nanoparticles was evaluated by Dynamic Light Scattering (DLS), which demonstrated that the hydrodynamic size of the different carriers remained essentially constant regardless of the nucleic acid employed (*ca*. 30–40 nm, Fig. 2c, red bars). The slight differences found might be ascribed to the nature of each nucleic acid. In consequence, these nanoparticles would present an appropriate size to be systemically administered as drug delivery systems (>10 nm to avoid renal clearance and <200 nm to reduce an immune response)[48]. Similarly, the Z-potential measurements revealed a slight reduction in the surface charge of all oligonucleotide-containing AuNPs compared to the unmodified counterpart, showing an average value of *ca*. -30 mV in all cases (Fig. 2d, red bars).

The same parameters (size and z-potential) were also assessed upon incubation of the nanoparticles with plasma. It is well accepted that nanoparticles behaviour in vivo is intrinsically dependent on their ability to avoid the immune system and to reach their target tissue or organ[49]. When nanoparticles are released into the bloodstream, they are immediately coated by a dynamic protein layer called the protein corona. This coating significantly affects pharmacokinetics, biodistribution, and target recognition of the therapeutic nanoparticles. We, therefore, measured the physicochemical properties of the different aptamer-conjugated AuNPs upon incubation with plasma, to allow the formation of a functional protein corona. As expected, the biomolecular corona increased the hydrodynamic size

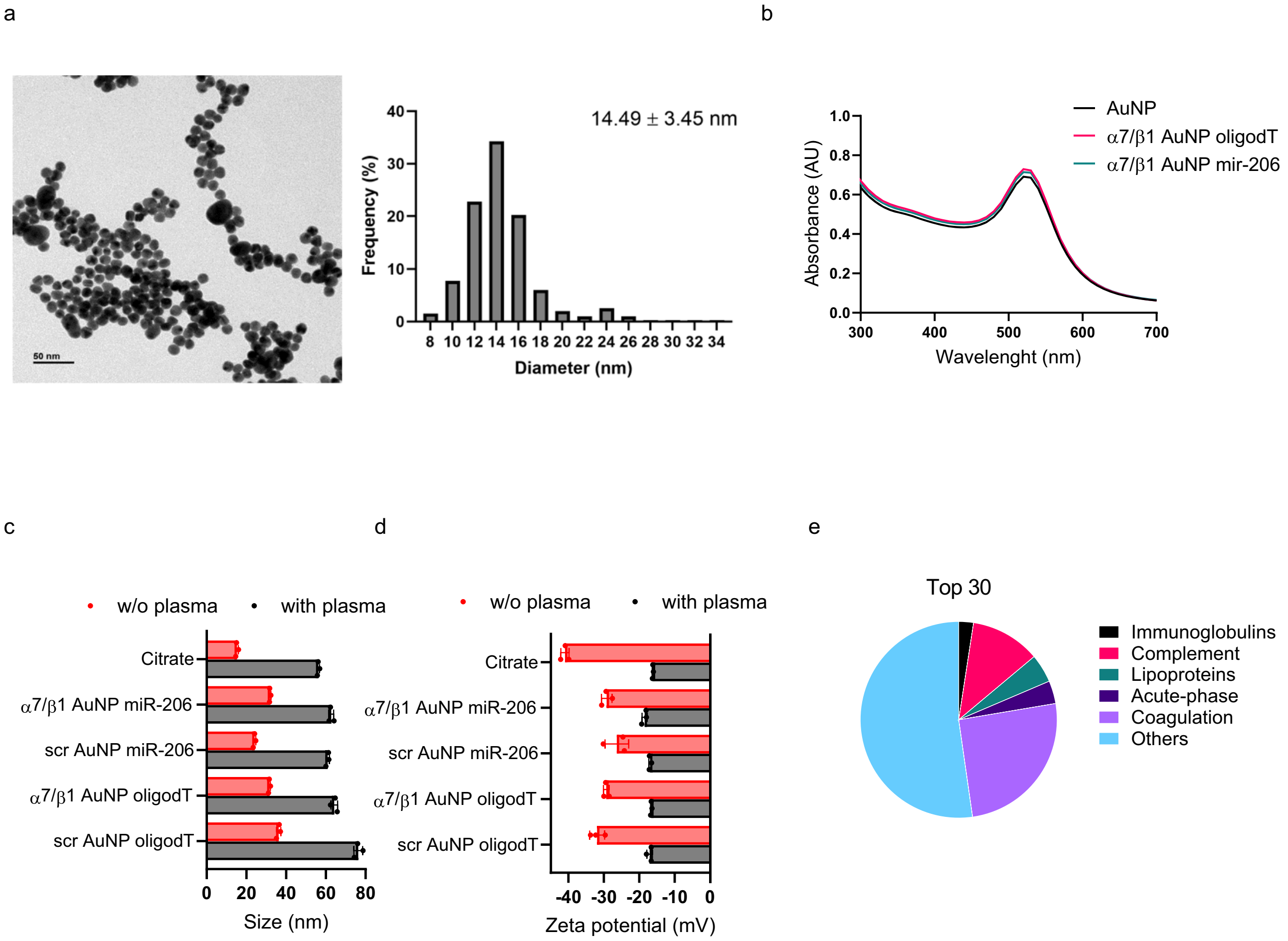

Fig. 2 | Aptamer-conjugated AuNPs containing oligonucleotides retain their physicochemical properties. a Transmission Electronic Microscopy (TEM) image of a representrative batch of gold nanoparticles (AuNPs). The histogram show the size distribution of the AuNPs, with a mean size of 14.49 ± 3.45 nm ($n = 400$ nanoparticles). Similar results were obtained with all the AuNPs batches used. **b** Absorbance spectrum of the different AuNPs formulations, where the corresponding surface resonance plasmon band is shown around 520 nm. **c** Dynamic Light Scattering (DLS) measurements of AuNPs in aqueous media (red) and after incubation with plasma (grey). Overall, size remained constant among groups (ca. 30 nm in aqueous medium; ca. 60 nm after incubation with plasma), regardless of the oligonucleotide composition. Data are presented as mean values +/- SD ($n = 3$ biological replicates). **d** Zeta potential measurements of AuNPs in aqueous media (red) and after incubation with plasma (grey). The surface charge was unaffected by the specific oligonucleotide attached (ca. -30 mV), showing a reduction of negativity after the protein coating in all cases (ca. -18 mV). Data are presented as mean values +/- D ($n = 3$ biological replicates). **e** Composition of the protein corona, considering the 30 more abundant proteins, according to their functional processes in plasma.

(Fig. 2c, grey bars) and decreased the z-potential (Fig. 2d, grey bars) of the functionalized AuNPs.

Protein corona composition of the therapeutic α7/β1 AuNPs miR-206 in dystrophic plasma

We next performed mass spectrometry analysis to investigate the identity of the proteins bound to the therapeutic AuNPs when exposed to plasma obtained from dystrophic mice (D2-mdx mice) (Supplementary Fig. 2a). The identified proteins were then grouped according to the described functional processes in plasma ("coagulation", "complement", "immunoglobulins", "lipoproteins", "acute phase", "lipoproteins" and "others") as reported in ref. 50. Annotation of the 30 (Fig. 2e) and 200 (Supplementary Fig. 2b) most abundant bound proteins show a very low percentage of immunoglobulins and lipoproteins in the protein corona formed when the α7/β1 AuNPs miR-206 were incubated with D2-mdx plasma. Immunoglobulins deposition on protein corona has been recently associated with complement opsonization and diminished efficiency of therapeutic nanoparticles[51]. These results suggest that the α7/β1 AuNPs miR-206 may have a low immunogenic profile. In addition, the ApoE lipoprotein, which is thought to be the main responsible for nanoparticle's liver targeting due to its ability to bind to low-density lipoprotein receptors present in liver cells, is barely present in the biomolecular corona (around 1%), suggesting the α7/β1 AuNPs miR-206 may have a low liver retention if delivered through the bloodstream. A list of the 30 more abundant proteins and their relative levels is shown in Supplementary Fig. 2c, while a list of the 200 more abundant proteins is shown in Supplementary Data 1.

In vitro treatment with α7/β1 AuNPs miR-206 stimulates differentiation of muscle cells

Having characterized the physicochemical properties of the functionalized AuNPs, we tested them in vitro, in C2C12 myoblasts. To assess for oligonucleotide intracellular delivery, we first used AuNPs containing a fluorescent oligonucleotide (oligodT-cy5). Results shown in Fig. 3a, b show that over 95% of C2C12 cells incorporate oligodT-cy5. Then, to investigate the ability of our nanoformulation to release a functional miRNA, we used a luciferase reporter assay. Briefly, we stably transfected C2C12 cells with a luciferase reporter containing the miR-206 seed sequence in the 3' UTR. As shown in Fig. 3c, α7/β1 AuNPs

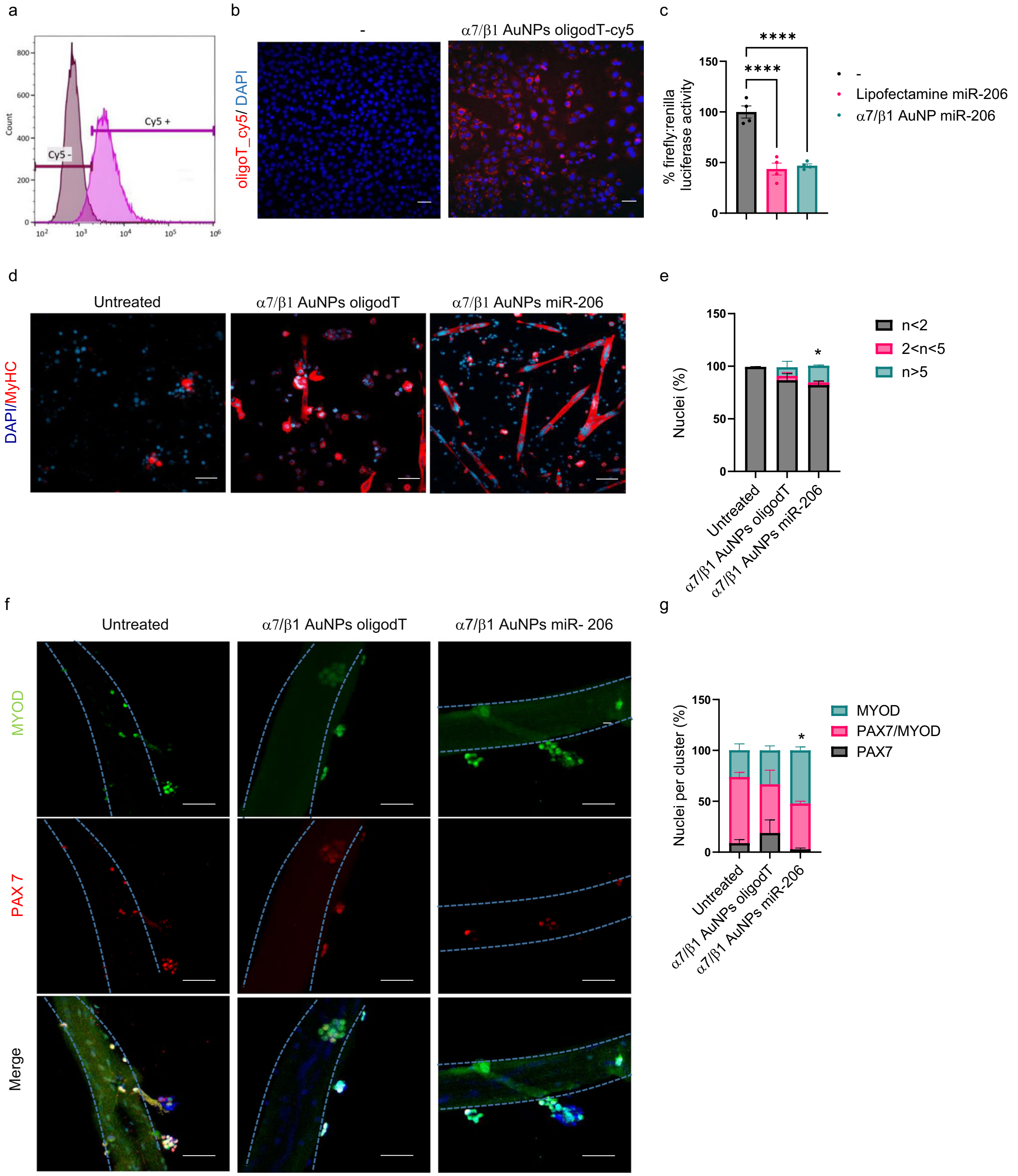

miR-206 efficiently release a functional miRNA, able to repress the luciferase reporter. The efficiency mimics the one obtained when miR-206 was transfected using lipofectamine. Of note, the AuNPs are not cytotoxic at doses at least three-fold higher than those used in all the in vitro experiments, as shown in Supplementary Fig. 3a.

We next investigated if functionalized AuNPs can deliver a functional miR-206 in dystrophic MuSCs. To this purpose, we isolated MuSCs by fluorescence-activated cell sorting (FACS), as CD31, CD45, TER119, SCA1-negative, ITGA7-positive mononuclear cells from D2-mdx muscles and treated them ex vivo with α7/β1 AuNPs containing miR-206 or control oligonucleotides. Previous work showed that miR-206 over-expression enhances MuSC ability to differentiate into myotubes[19] and stimulates MuSCs differentiation and fusion into muscle fibres in mdx mice[18]. Consistently, we observed that α7/β1 AuNPs miR-206 increases MuSC fusion into myotubes, when cultured in proliferation medium, as compared to cells either untreated or treated with control α7/β1 AuNPs (AuNPs oligodT) (Fig. 3d, e). In addition, treatment with control α7/β1 AuNP oligodT partially stimulates the differentiation of isolated MuSCs, even in the absence of miR-206, as shown by the slight increase in the number of myosin heavy chain (MyHC)-positive cells (Fig. 3d, e) and in the partial expression of early (*Myog*) and late (*Myh2*) differentiation markers (Supplementary

Fig. 3 | Aptamer-conjugated AuNPs efficiently deliver a functional miR-206 mimic and stimulate MuSCs differentiation ex vivo. a Cytofluorimetry and **b** fluorescence analysis of C2C12 cells treated with PBS or α7/β1 AuNPs containing oligodT-cy5 (3 nM) for 24 h. Scale bar: 50 μm. The histogram and panels show representative images of two independent experiments performed in triplicate. **c** Luciferase experiments performed in C2C12 cells containing the reporter plasmid pmirGLO 206 and transfected with miR-206 (5 μM) using lipofectamine, or treated with α7/β1 AuNPs functionalized with miR-206 (3 nM). Data are presented as mean values +/- SEM ($n = 4$ independent experiments). Statistical analysis was performed using one-way ANOVA followed by Tukey's *post hoc* test. **d** Immunofluorescence performed in MuSCs derived from D2-mdx mice isolated by FACS as lineage (CD31, CD45, TER119)-negative, SCA1-negative, ITGA7-positive and treated with the indicated AuNPs (3 nM) in growth medium. Red, MyHC (MF20), Blue, DAPI. Untreated cells are shown as a control. Scale bar: 70 μm. **e** Graph showing the percentage of nuclei contained in eMyHC- fibres containing 1, 2 to 5 or >5 nuclei in the same conditions as in (**c**). Data are presented as mean values +/- SEM ($n = 3$ biological replicates). Statistical analysis was performed using one-way ANOVA followed by Tukey's *post hoc* test. * indicates statistical differences between α7/β1 AuNPs miR-206 and untreated fibres. **f** Fluorescence analysis on freshly isolated myofibres using anti-PAX7 and anti-MYOD antibodies after 48 h in culture. Blue, DAPI. Scale bar: 50 μm. **g** Quantification of the percentage of PAX7, MYOD and PAX7/MYOD positive cells per cluster in (**f**). Data are presented as mean values +/- SEM ($n = 3$ independent experiments, with at least 30 clusters per per condition analysed in each experiment). Statistical analysis was performed using one-way ANOVA followed by Tukey's *post hoc* test. * indicates statistical differences in MYOD positive cells between α7/β1 AuNPs miR-206 and untreated fibres.

Fig. 3b). These results are in agreement with previously published work using gold- silver (Au-Ag) nanoparticles[52], suggesting that some inorganic nanoparticles may modulate both activation and differentiation of MuSCs by themselves[53]. Finally, we show here that α7/β1 AuNPs can modulate the activity of MuSCs also in their niche. To this end, we treated freshly isolated myofibres for 48 h with control or α7/β1 AuNPs miR-206 and stained them with antibodies recognizing MYOD and PAX7, two key markers of MuSCs function that mark the quiescent (PAX7 single positive) activated (PAX7/MYOD double positive), or committed (MYOD single positive) cellular stages of muscle differentiation[54]. Of note, Pax7 mRNA is a direct target of miR-206[55]. Our results show that miR-206-containing AuNPs stimulate MuSCs differentiation within the context of their niche, as shown by the decrease in the number of PAX/ MYOD positive cells in favour of an increase in the number of MYOD single-positive cells (Fig. 3f, g). Altogether, these data demonstrate that α7/β1 AuNPs containing miR-206 efficiently target skeletal muscle cells ex vivo and increase their differentiation potential.

Intramuscular injection of α7/β1 AuNPs miR-206 stimulates skeletal muscle regeneration in a mouse model of DMD

Next, we tested the effect of delivering the functionalized AuNPs in vivo into dystrophic muscles by local (intramuscular) injection. To this end, we first injected α7/β1 AuNPs oligodT-cy5 (AuNPs concentration: 33.6 nM; oligonucleotide dose: 0. 3 mg/kg) into the TA muscles of 8 weeks old D2-mdx mice and assessed for fluorescence release by confocal microscopy. Results shown in Supplementary Fig. 4 indicate that cy5 fluorescence is still observed within dystrophic muscles 1 week after the injection. However, we could not unequivocally discriminate if the muscle-resident cell population receiving the α7/β1 AuNPs oligodT-cy5 corresponded to PAX7-positive MuSCs, as the immunofluorescence protocol conditions inactivated the fluorescent dye.

We then injected α7/β1 AuNPs miR-206 or control α7/β1 AuNPs oligodT (AuNPs concentration: 33.6 nM; oligonucleotide dose: 0.3 mg/kg per injection), once a week for a total of 3 weeks (Fig. 4a). This treatment protocol was selected based on results shown in Supplementary Fig. 4 and on published work showing that MuSCs reacquire quiescence 5–7 after activation, following the formation of new myofibres[56]. We reasoned that delivering the therapeutic AuNPs once a week should be enough to allow a full cycle of MuSCs-mediated regeneration and return to quiescence, while keeping detectable levels of the oligonucleotide cargo. After the sacrifice, we performed histological analysis to assess AuNPs delivery into muscle-resident cells (Fig. 4b), miR-206 levels (Fig. 4c, d), skeletal muscle regeneration (Fig. 4e, f) and fibrotic deposition (Fig. 4g, h). Our results confirmed that local delivery of both α7/β1 AuNPs miR-206 and control α7/β1 AuNPs oligodT into TA muscles efficiently target muscle-resident cells (Fig. 4b) while, in addition, treatment with α7/β1 AuNPs miR-206 strongly increases the levels of this miRNA, which is highly enriched in the newly formed, centrally nucleated, myofibres (Fig. 4c, d, red arrows). Functionally, treatment with α7/β1 AuNPs miR-206 induces a strong increase in the number of regenerating embryonic MyHC (eMyHC)-positive fibres as compared to PBS-treated animals and mice injected with control AuNPs (Fig. 4e, f), with no changes in fibrotic deposition (Fig. 4g, h). Altogether, these data point out to a specific effect of the treatment on MuSC-mediated regeneration after local delivery of the therapeutic nanoparticles.

Systemic delivery of α7/β1 AuNPs efficiently target skeletal muscles, including MuSCs, in dystrophic mice

Given the strong pro-regenerative response observed after local delivery of miR-206 in D2-mdx mice, we next tested if the developed nanotherapy was suitable for systemic delivery. We first investigated if the α7/β1 AuNPs efficiently target dystrophic muscles when injected into the bloodstream. To this end, we injected 8-weeks old D2-mdx mice intravenously with AuNPs- oligodT-cy5 conjugated to either scr- or α7/β1 aptamers (AuNPs concentration: 33.6 nM, oligonucleotide concentration: 1.5 mg/kg). After 24 h we sacrificed the animals, harvested skeletal muscles (TA, gastrocnemius, quadriceps and triceps), lung, heart, liver, spleen, kidney and brain, and analysed the released fluorescence using an IVIS imaging system. Data shown in Fig. 5a, b show that α7/β1 AuNPs, but not those containing the control aptamer, efficiently target skeletal muscle tissue in dystrophic mice after intravenous injection. We also detected cy5 fluorescence in kidney and liver, but not in any of the other organs analysed. Liver, and to a lower extent kidney and spleen, have been previously described as the main organs involved in the clearance of oligonucleotide conjugated AuNPs[33,35], while kidney is also the primary organ for the clearance of small molecules, such as the unconjugated oligodT-cy5[57,58]. To discriminate if the strong fluorescent signal observed in the kidneys was due to the retention of conjugated AuNPs or the clearance of unconjugated cy5 fluorophores, we also measured the amount of gold deposition by Induced Couple Plasma mass spectrometry (ICP-MS). To this end, we injected 8-weeks old D2-mdx mice intravenously with AuNPs- oligodT conjugated to either scr- or α7/β1 aptamers (AuNPs concentration: 33.6 nM). Twenty four hours after the treatment, we harvested skeletal muscle, heart, liver, spleen, and kidneys for ICP-MS analysis to quantitate metal deposition in the different organs[59]. Data shown in Fig. 5c confirmed that α7/β1 AuNPs efficiently target skeletal muscle tissue 24 h after intravenous injection. Scramble-AuNPs, on the contrary, do not efficiently reach skeletal muscle tissues and preferentially accumulate in the liver and, to a lesser extent, in the spleen and kidney after systemic delivery, as previously observed for other oligonucleotide-conjugated AuNPs of the same size[35,36]. These results indicate that the α7/β1 aptamer strongly improves skeletal muscle delivery of oligonucleotide conjugated AuNPs in dystrophic mice after intravenous injection.

We next investigated if the α7/β1 AuNPs were able to target also MuSCs within dystrophic muscles. To this end we delivered α7/β1

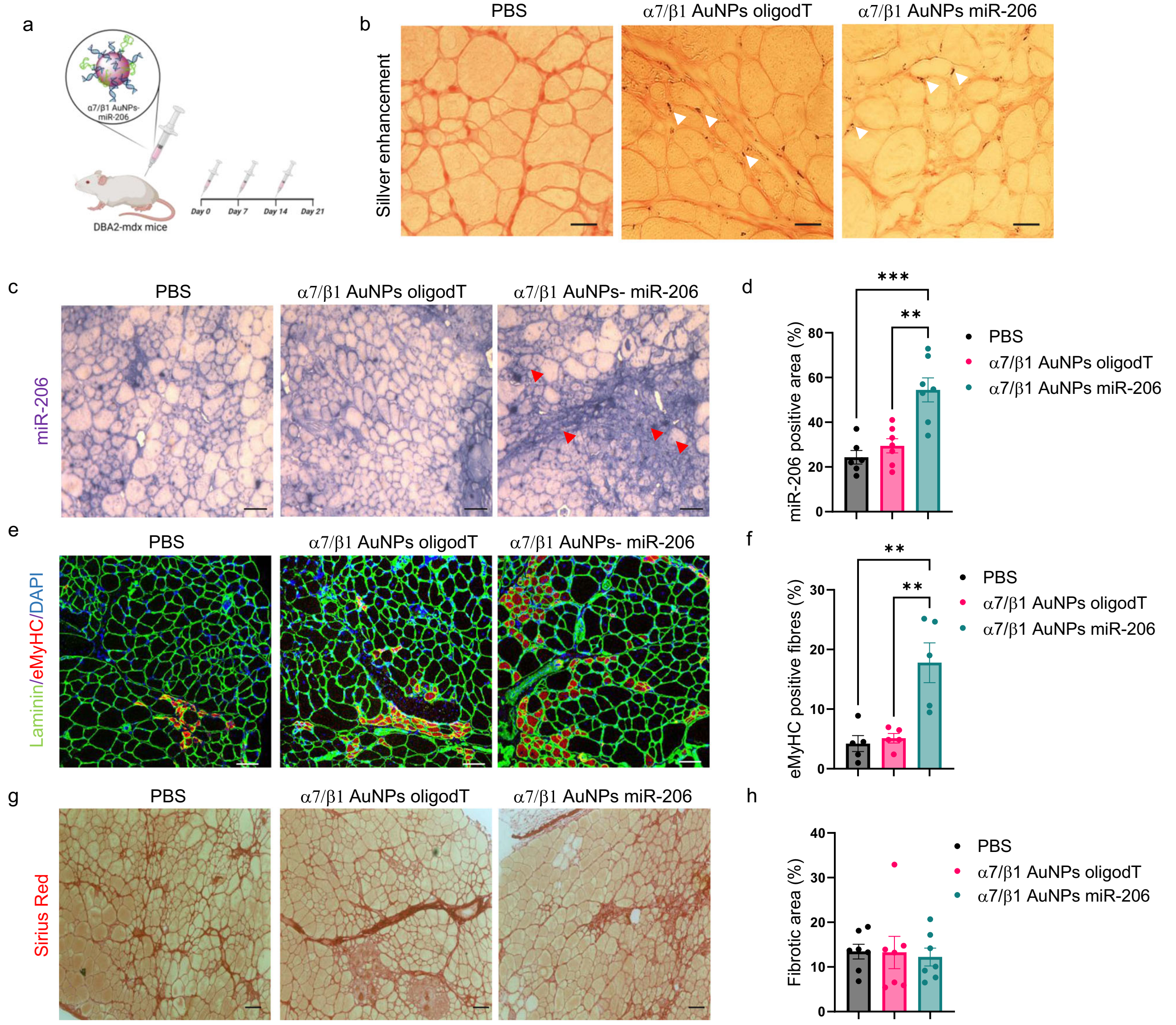

Fig. 4 | Functionalized AuNPs efficiently stimulate muscle regeneration in D2-mdx mice when injected locally. a Scheme of the experimental protocol. **b** Silver enhancement performed on transversal sections on TA muscles of mice treated once a week for a total of 3 weeks with intramuscular injections of either PBS, α7/β1 AuNPs containing oligodT or α7/β1 AuNPs containing miR-206. White arrows indicate AuNP deposition. Scale bar: 30 μm. The panels show representative images of three independent muscles. **c** miR-206 staining in TA muscles of mice treated as in (**b**). Red arrows indicate miR-206 within centrally nucleated, regenerating, myofibres. Scale bar: 50 μm. **d** Graph shows the percentage of stained area (in pixels) quantified in (**c**). Data are presented as mean values +/- SEM ($n = 7$ biological replicates). **e** Immunofluorescence for embryonic myosin heavy chain (eMyHC-red) and laminin (green) in the same conditions as in (**b**). Nuclei were counterstained with DAPI (blue). Scale bar: 50 μm. **f** Graph shows the percentage of eMyHC positive fibres. Data are presented as mean values +/- SEM (n = 5 biological replicates)**. g** Sirius red staining performed on TA muscles. Scale bar: 50 μm. **h** Graph shows the percentage of fibrotic area in the different conditions. Data are presented as mean values +/- SEM ($n = 7$ biological replicates). Statistical analysis was performed using one-way ANOVA followed by Tukey's *post hoc* test in all panels. Figure 4a was created in BioRender. Somoza, Á. (2024). https://BioRender.com/w38k062.

AuNPs oligodT-cy5 via intravenous injection as in Fig. 5a, b and 24 h later we harvested hindlimb muscles for cytofluorimetry analysis, using antibodies against CD31, CD45, TER119, SCA1 and ITGA7 for lineage determination. The results shown in Fig. 5d show cy5 fluorescence in around 20% of MuSCs after a single intravenous injection with the indicated AuNPs. No fluorescence was observed in FAPs or in hematopoietic and endothelial cells (labelled as lineage positive in the graph) further corroborating the selectivity of our system towards the muscle lineage.

Unexpectedly, we did not detect α7/β1 AuNPs accumulation in the heart with any of the methodologies used (IVIS, Fig. 5a, b and ICP-MS, Fig. 5c). Lack of accumulation in the heart was surprising, as the α7/β1 integrin dimers we previously described to be expressed also in cardiac tissue[40,41]. To investigate if the preferred selectivity towards skeletal muscle could be due to the presence of different levels of α7/β1 integrin in the two tissues in dystrophic mice, we performed immunofluorescence analysis using antibodies against α7 and β1 integrins. Results shown in Supplementary Fig. 5a show that the levels of the two integrins are barely detectable in cardiac muscle derived from D2-mdx mice as compared to skeletal muscle. In agreement with this observation, incubation with 5′ labelled α7/β1 aptamer does not efficiently label cardiac tissue in these mice (Supplementary Fig. 5b). Of note, both integrins are present in all the skeletal muscles analysed (Supplementary Fig. 5c).

Finally, to assess if our α7/β1 AuNP can also target highly inaccessible muscles, such as the diaphragm, and if they could be suitable for in vivo systemic delivery of miRNAs mimics, we injected D2-mdx

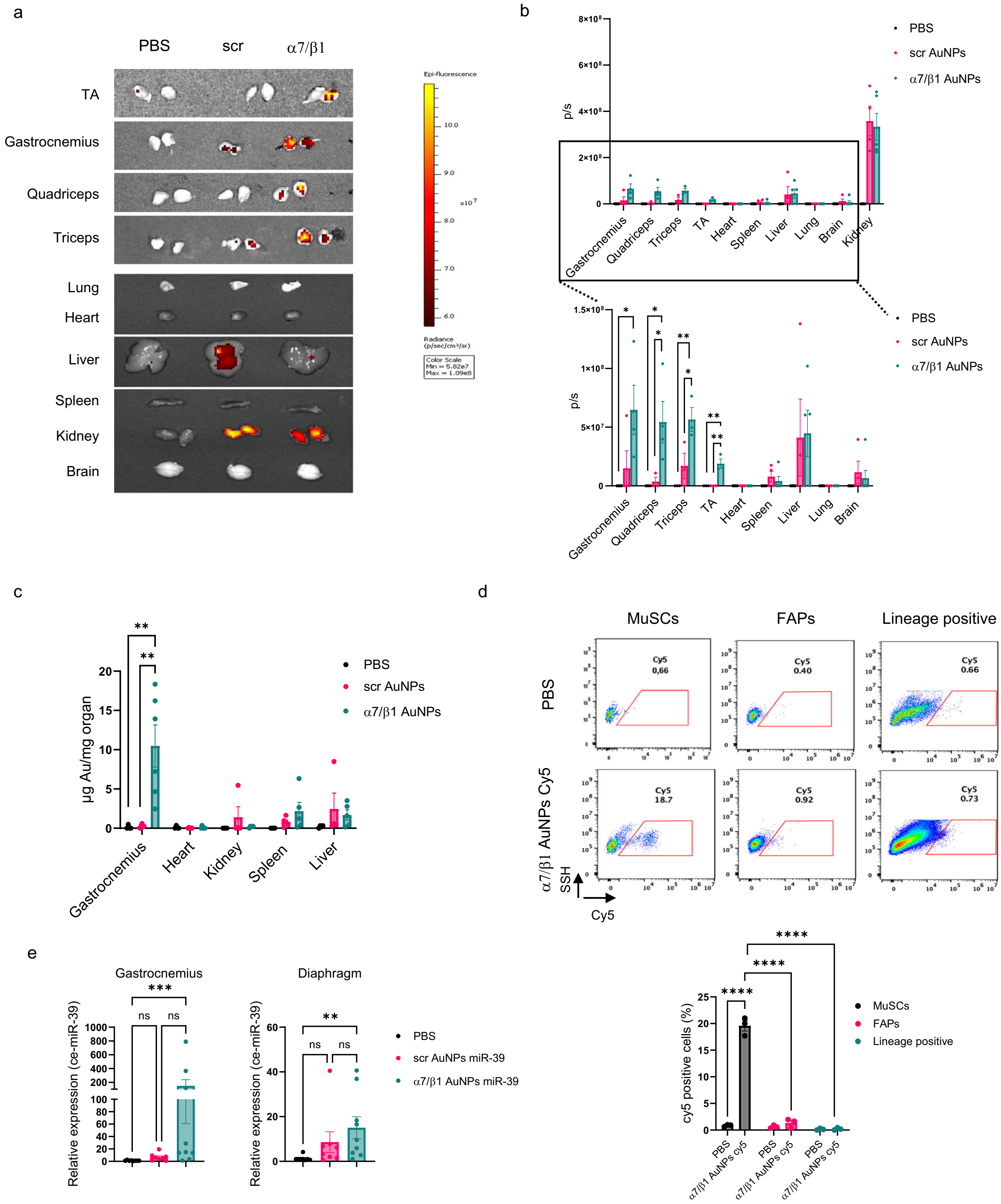

mice with scr- or α7/β1 AuNPs conjugated to a *C. elegans* specific miRNA, ce-miR-39. This miRNA was initially used instead of miR-206 to avoid interference with endogenous miRNAs, as it is not expressed in any *Mus musculus* tissue. The results shown in Fig. 5e confirmed that α7/β1 AuNPs can efficiently reach skeletal muscle (both hindlimb muscles and diaphragm) 24 h after injection, delivering as a cargo an exogenous ce-miR-39 and confirming the validity of our system as an efficient platform for miRNA release into skeletal muscle tissue of dystrophic mice.

Systemic delivery of α7/β1 AuNPs miR-206 stimulates skeletal muscle regeneration and improves muscle functionality in D2-mdx mice

Once assessed that the α7/β1 AuNPs efficiently target skeletal muscle and can be used for the delivery of miRNA mimics, we investigated whether systemic treatment with α7/β1 AuNPs containing the therapeutic miRNA miR-206 promotes skeletal muscle regeneration and functional recovery in dystrophic mice. To this end, we treated 8-weeks old D2-mdx mice with aptamer-conjugated AuNPs containing

Fig. 5 | α7/β1 AuNPs efficiently target skeletal muscles, including the diaphragm, when injected into the bloodstream. a Fluorescence imaging (IVIS) of the indicated muscles and organs 24 h after a single IV injection of α7/β1 or scramble AuNPs containing oligodT-cy5. PBS-treated animals are used as a negative control. **b** Signal intensity measured as photons per second (p/s) Data are presented as mean values +/- SEM ($n = 4$ biological replicates). Statistical analysis was performed using one-way ANOVA followed by Tukey's *post hoc* test. **c** ICP-MS on gastrocnemius, heart, kidney, liver and spleen isolated from in D2-mdx mice 24 h after systemic delivery of α7/β1 or scramble AuNPs. Graph show the normalized amount of gold (in µg) per organ weight. Data are presented as mean values +/- SEM ($n = 5$ biological replicates). Statistical analysis was performed using two-way ANOVA followed by Tukey's *post hoc* test. **d** Representative flow cytometry plot showing the amount of cy5-positive cells on MuSCs, FAPs and lineage-positive cells after a single IV injection of α7/β1 AuNPs cy5. Graph shows the percentage of cy5-positive cells in the different populations. Data are presented as mean values +/- SEM ($n = 3$ biological replicates). Statistical analysis was performed using two-way ANOVA followed by Tukey's *post hoc* test**. e** qRT-PCR showing the relative levels of ce-miR-39 normalized against the small nuclear RNA U6 in the gastrocnemius and diaphragm of D2-mdx mice after systemic delivery of α7/β1 or scramble AuNPs miR-39. PBS-treated mice are used as a control. Data are presented as mean values +/- SEM ($n = 8$ biological replicates). Statistical analysis was performed using one-way ANOVA followed by Kruskal-Willis *post hoc* test.

either miR-206 or a control oligonucleotide (oligodT), once a week for up to 5 weeks (AuNPs concentration: 33.6 nM; final oligonucleotide dose: 0.75 mg/kg per injection). We first confirmed by qRT-PCR experiments that α7/β1 AuNPs miR-206 efficiently target skeletal muscles when injected in the caudal vein. Our results show an increase in miR-206 levels in hindlimb muscles (quadriceps) (Supplementary Fig. 6a) and diaphragm (Supplementary Fig. 6b) isolated from α7/β1 AuNP miR-206 treated mice, as compared to control AuNPs and PBS-treated animals. Moreover, we confirmed that α7/β1 AuNPs selectively target MuSCs, as shown by the increase in miR-206 levels in those cells, but not in other muscle-resident populations, such as FAPs or macrophages, that were co-isolated by FACS (Fig. 6a). We also observed that control AuNPs (which do not contain miR-206) could partially stimulate the expression of endogenous miR-206 both in hindlimb skeletal muscle (Supplementary Fig. 6a) and in MuSCs (Fig. 6a). This observation is consistent with our ex vivo data showing partial stimulation of MuSCs with α7/β1 AuNPs oligodT (Fig. 3c, d) and is probably due to the intrinsic ability of AuNPs to activate muscle cells[52].

Then, we investigated the effect of systemic treatment with α7/β1 AuNPs miR-206 on skeletal muscle regeneration and functional recovery in D2-mdx mice. Immunofluorescence analysis in gastrocnemius, quadriceps, triceps, TA, and diaphragm showed that intravenous delivery of α7/β1 AuNPs miR-206 induces a significant increase in the number of regenerating eMyHC-positive fibres, as compared to PBS-treated animals and mice injected with control AuNPs (α7/β1 AuNPs oligodT) (Fig. 6b, c and Supplementary Fig. 7). On the other hand the number of fibres per section, as well as their average calibre, remained unchanged within the different experimental groups (Supplementary Fig. 8). Moreover, the increase in the number of regenerating myofibres does not correlate with an increase in tissue necrosis (Supplementary Fig. 9), suggesting that regeneration is not due to an exacerbated muscle damage due to the treatment but instead to the ability of the released miR-206 to stimulate MuSCs-mediated regeneration. Moreover, consistent with a highly selective effect of the treatment towards the skeletal muscle lineage, we did not observe any change in the amount of fibrotic deposition (Supplementary Fig. 10).

Finally, to demonstrate that the increased regeneration has a functional outcome on muscle functionality and strength, we performed a forelimb grip strengh test. For these experiments, mice were treated once a week, for 5 weeks, with intravenous delivery of α7/β1 AuNPs oligodT, α7/β1 AuNPs miR-206 or PBS. Forelimb strength was measured once a week using a grip strength meter (Bioseb Bio GS-3) and normalized by the weight of the animal. The results show that treatment with α7/β1 AuNPs miR-206 increases maximal normalized strength (Fmax) as compared to control animals treated with either PBS or with α7/β1 AuNPs oligodT (Fig. 6d). While longer treatments will be needed to define the long-term effect and therapeutic window of action better, altogether these results demonstrate that systemic delivery of α7/β1 AuNPs efficiently target MuSCs, stimulating their regeneration potential and improving the functionality of dystrophic muscles.

α7/β1 AuNPs have an intrinsic ability to stimulate MuSCs proliferation

To get mechanistic insights on α7/β1 AuNPs miR-206 mechanism of action, and to address if increased muscle regeneration is due to the ability of the α7/β1 AuNPs miR-206 to modulate MuSCs function in vivo, we performed immunofluorescence experiments on transversal muscle sections of gastrocnemius muscles using antibodies against PAX7, MYOD and the proliferation marker KI67. Our data show that treatment with α7/β1 AuNPs (either oligodT or miR-206) does not significantly change the total number of PAX7-positive MuSCs per fibre as compared to PBS-treated animals (Fig. 7a, b) but increases the percentage of proliferating, KI67/PAX7 double positive MuSCs (Fig. 7c). This indicates that the α7/β1 AuNPs per se can activate the MuSCs compartment in dystrophic mice, without leading to an exhaustion of the MuSCs compartment in the timeframe analyzed. Moreover, treatment with α7/β1 AuNPs miR-206, but not with α7/β1 AuNP oligodT, increases the percentage of MYOD/PAX7 double positive MuSCs (Fig. 7d, e), showing that the released miR-206 can induce MuSCs differentiation, as expected from our ex vivo data (Fig. 3). This was further confirmed by measuring the differentiation index of MuSCs isolated from control or α7/β1 AuNPs miR-206 treated animals. The results shown in Supplementary Fig. 11 show that in vivo treatment with α7/β1 AuNPs miR-206 through systemic delivery increases the in vitro differentiation potential of isolated MuSCs, measured as the percentage of nuclei contained in MyHC-positive myofibres.

The results shown so far indicate that systemic delivery of aptamer-conjugated AuNPs containing miR-206 increases skeletal muscle regeneration in dystrophic mice, through modulation of both MuSCs proliferation (mediated by the AuNP) and differentiation (mediated by the cargo, miR-206).

α7/β1 AuNPs present a safety profile compatible with repetitive dosing

We finally assessed the safety profile of our nanoplatform. It is generally accepted that AuNPs are non-toxic, and some of them are currently under investigation in clinical trials[33–36]. However, given the need for repetitive dosing in our model, we checked if the treatment scheme and doses used to obtain a functional effect with our α7/β1 AuNPs (Fig. 6d) may have a detrimental effect on the animals due to accumulated toxicity. To this end, we measured animal welfare and growth during the whole duration of the experiments, and we performed histological analysis of different organs after 5 weeks of treatment. Our results confirmed that weekly treatment with aptamer-conjugated AuNPs (AuNPs concentration: 33.6 nM; oligonucleotide dose: 0.75 mg/kg per injection) did not lead to alterations in overall animal growth (Supplementary Fig. 12a) and did not show any sign of toxicity in organs such as liver and kidney, the main organs for AuNPs and oligonucleotide clearance, respectively (Supplementary Fig. 12b).

We also investigated if treatment with the α7/β1 AuNPs alters the inflammatory infiltrate in dystrophic muscles. Flow cytometry analysis showed that treatment with either control or α7/β1 AuNPs miR-206, injected systemically does not modulate the overall recruitment of

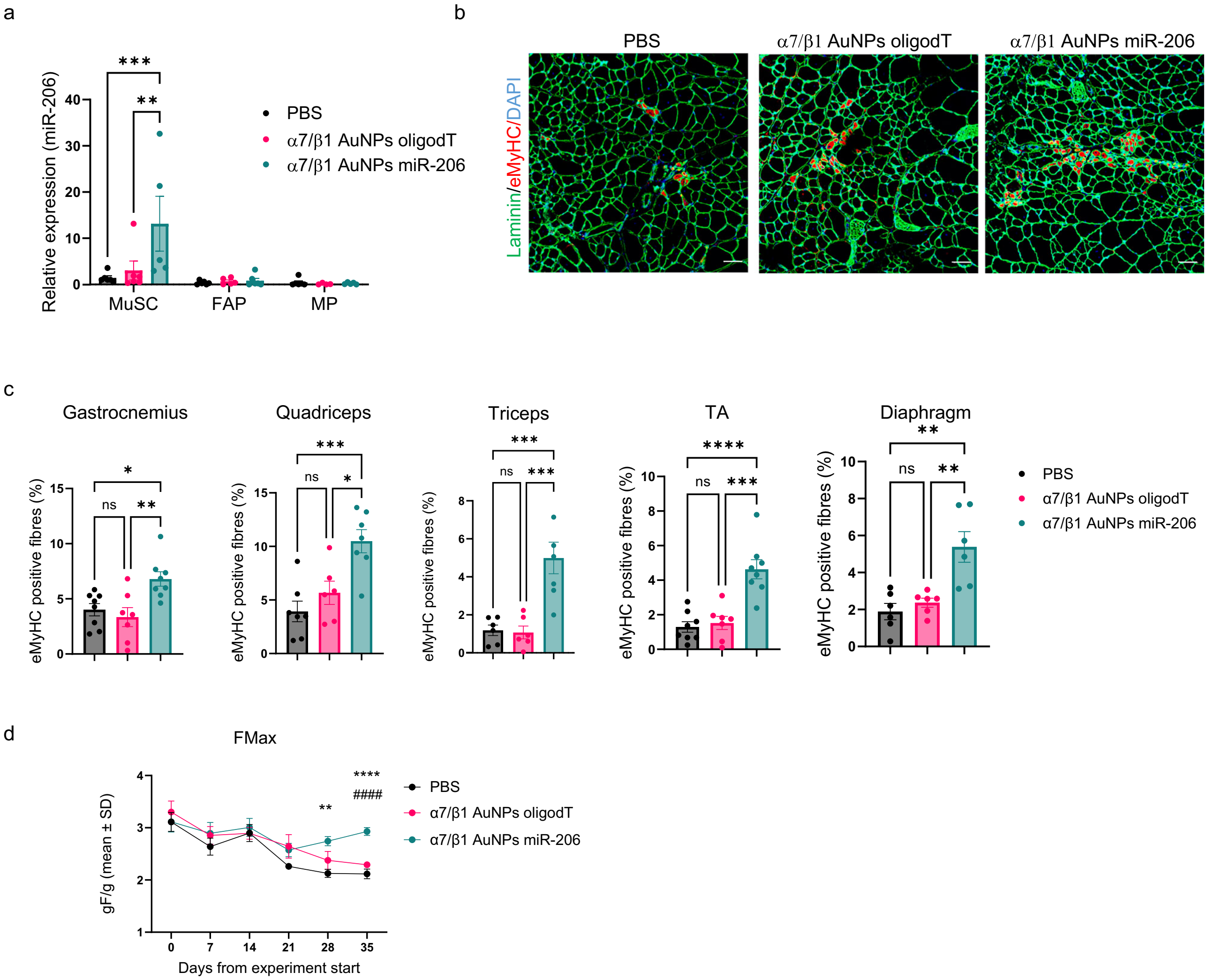

Fig. 6 | α7/β1 AuNPs miR-206 selectively target MuSCs in dystrophic mice, stimulate muscle regeneration and improve muscle function. **a** qRT-PCR showing the levels of miR-206 normalized against the levels of endogenous small nuclear RNA U6 in the indicated muscle-resident cell populations. Cells were isolated by FACS from gastrocnemius muscles of dystrophic mice treated via intravenous injection with PBS or with control or α7/β1 AuNPs miR-206 for 3 weeks. Data are presented as mean values +/- SEM ($n = 5$ animals per group). **b** Immunofluorescence staining for eMyHC-(red) and laminin (green) in skeletal muscle (gastrocnemius) of mice treated via intravenous injections of the indicated AuNPs, once a week for 5 weeks. Nuclei were counterstained with DAPI (blue). Scale bar: 50 µm. **c** Graph shows the quantifications of the percentage of eMyHC positive fibres in the gastrocnemius, quadriceps, triceps, TA and diaphragm of the same mice as in (**b**). Data are presented as mean values +/- SEM ($n = 8$ biological replicates for the gastrocnemius and tibialis; $n = 6$ for the quadriceps, triceps and diaphragm). **d** Graph showing the normalized maximal strength (Fmax) of the same animals as in (**b**). Data are presented as mean values +/- SEM ($n = 8$ biological replicates). Statistical analysis was performed using one-way ANOVA followed by Tukey's *post hoc* test in all panels. In panel (**d**) **** indicates statistically significant differences between α7/β1 AuNPs miR-206 and untreated animals; #### indicates statistically significant differences between α7/β1 AuNPs miR-206 and α7/β1 AuNPs oligodT.

hematopoietic cells to dystrophic muscles (Fig. 8a, b), or the percentage of F4/80 CD11b double positive cells, representing the macrophage population (Fig. 8c, d). Immunofluorescence analysis confirmed these data, showing that the percentage of F4/80 positive area in dystrophic muscles is not altered by the treatments (Fig. 8e, f).

In summary, our data show that the muscle selective nanoplatform described here represents a suitable delivery system for oligonucleotide release into dystrophic MuSCs. Such platform, which allows repetitive dosing without eliciting a toxic or immunogenic response, was successfully used to deliver miRNAs mimics (ie. miR206) in a mouse model of DMD. Systemic treatment through intravenous delivery of the α7/β1 AuNP-miR206 stimulated muscle regeneration in D2-mdx mice, leading to a functional recovery of muscle strength. Mechanistically, our results show that this is achieved through a combined effect of the nanotherapy in the modulation of the proliferation and differentiation potential of MuSCs.

Discussion

The delivery of therapeutic oligonucleotides is a promising strategy for many muscle disorders. However, it presents several caveats, including low in vivo stability, uneven efficacy, and poor targeting of skeletal muscle tissue[6]. While some issues, like nucleic acid stability, can be addressed through chemical modifications[60], efficacy highly depends on selective and efficient tissue targeting. In the case of skeletal muscle, this is particularly challenging, due to the extent of the target tissue and the need to reach all muscles in the body. Different types of nanoparticles have been tested in the past few years as delivery systems for muscle disorders, and the first proof-of-principles in animal models are now showing promising results[53,61]. Despite these studies strongly support the idea that conjugating oligonucleotides to a wide array of nanocarriers may improve their bioavailability and therapeutic action, efficient tissue up-taking and MuSCs targeting still needs to be solved.

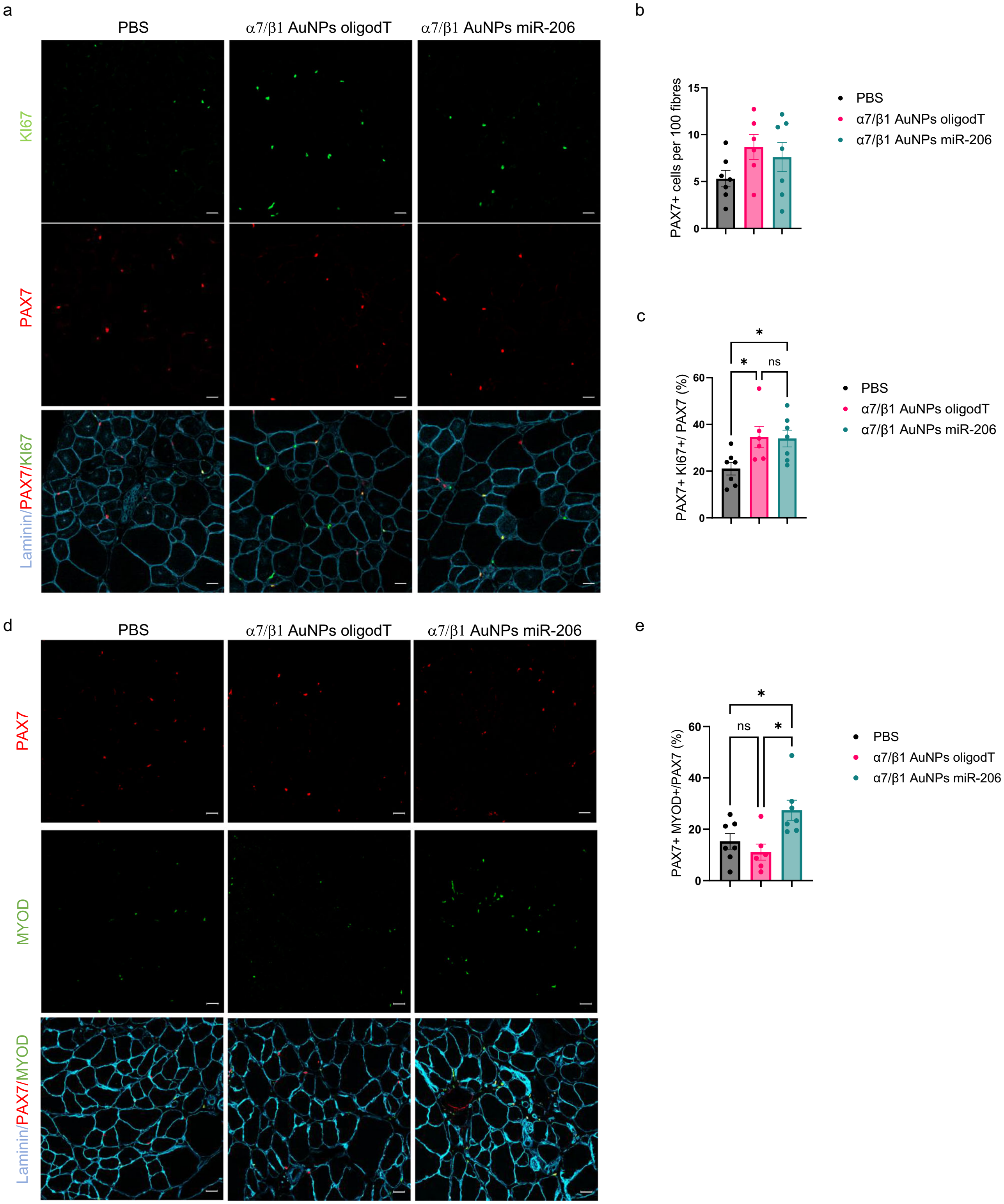

Fig. 7 | α7/β1 AuNPs stimulate MuSCs proliferation in a cargo-independent manner. a Immunofluorescence for PAX7 (red) and KI67 (green) staining in gastrocnemius of D2-mdx mice treated with intra-venous injections of PBS, α7/β1 AuNPs oligodT or α7/β1 AuNPs miR-206 (*n* = 7 per group). Nuclei were counter-stained with DAPI (blue). Scale bar: 20 μm. **b** Graph showing the number of PAX7-positive cells per 100 fibres in (**a**). Data are presented as mean values +/- SEM (*n* = 7 biological replicates per group). **c** Graphs showing percentage of KI67/ /PAX7-double positive cells over total PAX/7-positive cells. Data are presented as mean values +/- SEM (*n* = 7 biological replicates per group). **d** Immunofluorescence for PAX7 (red) and MYOD (green) staining in gastrocnemius of D2-mdx mice treated with intravenous injections of PBS, α7/β1 AuNPs oligodT or α7/β1 AuNPs miR-206. Scale bar: 20 μm (**e**) Graphs showing percentage of MYOD//PAX7-double positive cells over total PAX/7-positive cells. Data are presented as mean values +/- SEM (*n* = 7 biological replicates per group). Statistical analysis was performed using one-way ANOVA followed by Tukey's *post hoc* test in all panels.

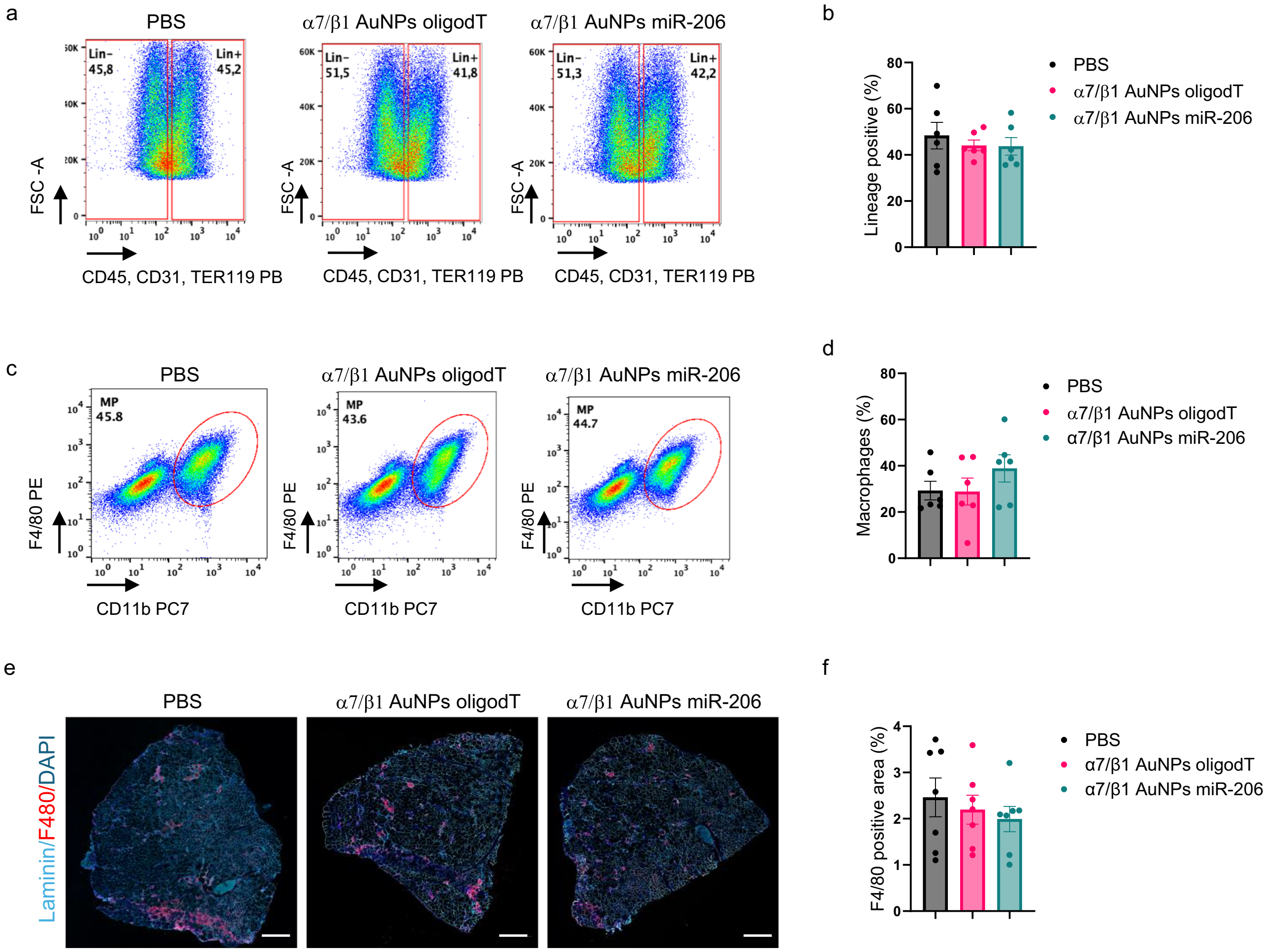

Fig. 8 | Systemic treatment with α7/β1 AuNPs miR-206 does not alter the inflammatory infiltrate in D2-mdx mice. a Representative flow cytometry plot showing lineage (CD45, CD31, TER 119) positive and negative cells on gastrocnemius muscles obtained from mice treated with PBS, α7/β1 AuNPs oligodT or α7/β1 AuNPs miR-206. **b** Percentage of lineage positive cells in the different conditions, analyzed by flow cytometry in (**a**) ($n = 6$). **c** Representative flow cytometry plot showing F4/80 and CD11b positive cells (macrophages) on the lineage-positive population described in (**a**). **d** Percentage of F4/80 and CD11b positive cells over the total lineage positive cells, analyzed by flow cytometry in (**c**). Data are presented as mean values +/- SEM ($n = 6$ biological replicates). **e** Immunofluorescence staining for F4/80 (red) and laminin (cyan) in the gastrocnemius of mice treated via intravenous injection with PBS or with control or α7/β1 AuNPs miR-206. Scale bar: 500 µm. **f** Graph shows the percentage of F4/80-positive area in the different conditions. Data are presented as mean values +/- SEM ($n = 7$ biological replicates). Statistical analysis was performed using one-way ANOVA followed by Tukey's *post hoc* test in all panels (no statistically significant differences were observed).

Tissue selectivity can be achieved using muscle-targeting molecules, such as peptides, antibodies, enzymes, or aptamers[62,63]. Some of these molecules have been tested in cell lines[64,65], or in vivo[66,67]. However, none of these strategies has proven effective in targeting MuSCs, the cells responsible for muscle regeneration. Recently, a groundbreaking work from Millay's lab demonstrated that engineered lentiviruses containing muscle fusogenic genes can target activated MuSCs and can be used for muscle gene delivery[68]. However, although viral vectors are commonly used in gene therapy, there are still concerns regarding their safety, including immunogenicity or, in the case of lentiviruses, random integration within the genome.

Here, we describe a muscle-targeting aptamer that can be used in combination with nanoparticles for the selective delivery of therapeutic oligonucleotides into skeletal muscle tissue, with a high affinity for the MuSCs compartment. Aptamers are a class of nucleic acid ligands, with usually a high binding affinity to the target molecule[69]. The muscle-targeting aptamer described here was designed against the α7/β1 integrin dimer, a surface protein highly enriched in striated muscles[40,41]. Consistently with the α7/β1 integrin expression patterns, Alexa594 5′ end-labelled α7/β1 aptamer efficiently recognizes skeletal muscle fibres and MuSCs both in transversal muscle sections, bulk muscle-resident cell populations, and isolated single myofibres. Recently, another muscle-specific aptamer was identified using a cell internalization SELEX process. This aptamer was shown to internalize into muscle fibres when injected locally in the TA muscle. However, the specificity of this aptamer upon systemic delivery, and its ability to target the MuSC compartment have not been addressed[70].

In this work, we show that α7/β1 aptamer-conjugated AuNPs efficiently target MuSCs and restore their ability to regenerate dystrophic muscles, after either local or systemic delivery in D2-mdx mice. D2-mdx mice were used in this work due to their more severe dystrophic phenotype as compared to mdx in the C57/Bl10 background[14]. Conjugation of the therapeutic miR-206, a muscle-specific miRNA that stimulates MuSCs function through a paracrine mechanism[25], improves skeletal muscle regeneration in dystrophic mice. On the other hand, it does not affect other histopathological parameters, such as necrosis, inflammation, or fibrotic deposition. This is not surprising as our data show that the α7/β1 AuNPs are not cytotoxic and do not target other muscle-resident cell populations, such as FAPs or immune cells. Although it was previously shown that MuSC-derived miR-206 plays an anti-fibrotic role in response to hypertrophic stimuli[71], our data demonstrate that this is not the case when miR-206 is delivered ectopically into dystrophic MuSCs.

On the other hand, despite α7/β1 integrin was previously described to be expressed in cardiac muscle, our biodistribution experiments using two different methodologies did not show a consistent accumulation of α7/β1 AuNPs in this tissue. Moreover, the results shown in this work suggest that the preferred selectivity towards skeletal muscle could be due to different levels of α7/β1 integrin dimers in the two tissues. In particular, while α7 and β1 integrin are present in skeletal muscle fibres and MuSCs, this integrin dimer is undetectable in cardiac tissues in the model used, the dystrophic D2-mdx mice. However, further studies are needed to investigate if the difference in the levels of these proteins is species or strain specific.

In addition to the targeting aptamer, a second advantage of the developed nanoplatform arises from its tailored design, based on the use of thiol bonds for oligonucleotide incorporation. This leads to preferential intracellular release, which is mediated by the high glutathione (GSH) levels[72]. GSH inside the cells is found within the range of 0.5–10 mM, with the higher levels observed in liver and skeletal muscle, whereas extracellular values are one to three orders of magnitude lower[73–75]. This GSH-dependent release, combined with the muscle-specific α7/β1 aptamer, allowed selective release of a functional miR-206 mimic into muscle cells, upon intravenous injection of the functionalized AuNPs[76].

Finally, a common bottleneck when exploring the use of inorganic nanoparticles for therapeutic purposes regards their safety profile. In this sense, AuNPs stem out as a versatile delivery system due to their almost absence of toxicity and low immunogenicity[77], which has led to the initiation of several clinical trials and FDA approval for medical applications[78]. This is consistent with our results showing that α7/β1 AuNPs containing miR-206 did not alter mice growth, nor induce alterations in organs such as liver and kidney. In addition, the treatment did not target or modulate the activity of muscle-resident macrophages. Although we have not fully addressed it here, the pharmacokinetics and safety profile of similar AuNPs in mice have been studied by other groups[35,36,79].

Despite being highly inert from an immunogenic profile, our data show that in vivo treatment with control nanoparticles, which do not contain the therapeutic miRNA, is enough to promote activation of MuSCs in dystrophic mice, as shown by the increase in the number of PAX7/KI67 double positive MuSCs with both α7/β1 AuNP oligodT and α7/β1 AuNP miR-206. Moreover, we also observed a slight (although not statistically significative) increase in the number of regenerating fibres when treating with control α7/β1 AuNP as compared to PBS in some of the muscles analysed. This is then further increased when the α7/β1 AuNP deliver a functional miR-206. Similar results were observed ex vivo when we treated freshly isolated MuSCs cells with α7/β1 AuNPs oligodT. These observations are consistent with published data showing that internalization of gold, and gold-silver nanoparticles enhances myogenic differentiation and promotes muscle regeneration in vivo[52]. It was previously shown that enhanced myogenic differentiation by such nanoparticles was dependent on activation of the p38α signalling pathway[52], a key cascade regulating MuSCs function and skeletal muscle regeneration[54]. Although further studies are necessary to elucidate the mechanisms of action on MuSCs activation by the α7/β1 AuNPs described here, our data suggest that our nanoplatform could have a positive role in regulating MuSCs function by itself, which is then further potentiated by their therapeutic cargo.

Altogether, the results presented here point out to the first directed nanoplatform that efficiently targets MuSCs when delivered systemically. We demonstrate here that aptamer-modified AuNPs can be used to deliver oligonucleotides into skeletal muscle in vivo, increasing muscle regeneration and improving muscle functionality in a mouse model of DMD. While in this work we delivered the therapeutic miR-206 mimic as a proof-of-principle, the versatility of our nanoplatform stems from the possibility of conjugating different types of oligonucleotides, such as antagomiRs, ASOs, or siRNAs, therefore amplifying its potential as a suitable delivery platform for a wide array of therapeutic molecules for muscle disorders.

Methods

SELEX experiments

Cross-over SELEX with random region of 40 deoxyribonucleotides (A,T,G,C) was carried out. DNA aptamer library containing ~10^{14} random oligonucleotides were considered as a starting pool for this SELEX. The sequence of the aptamer library is: 5′ GCCTGTTGTGAGCCTCCTGTCGAA –N40- TTG AGC GTT TAT TCT TGT CTC CC 3′ and forward primer 5′- GCC TGT TGT GAG CCT CCT GTC GAA -3′ and reverse primer 5′- GGGAGACAAGAATAAACGCTCAA -3′ to amplify eluted pools after each round. We have started with 500 picomoles of aptamer library and 10 picomoles of histidine tagged integrin α7/β1 which was immobilized on Ni-NTA beads. His-GST protein was used as a counter selection in each protein-SELEX round. After initial 4 rounds of protein SELEX, we moved to cell SELEX where around 7.5×10^6 C2C12 cells were used. As the rounds proceeded, selection pressure was introduced by varying the pool and target ratio and more stringent washing conditions. After 14 rounds of the evolution process, we have sequenced each pool by Illumina Next Generation sequencing (NGS). We obtained 89% to 95% of the pool which are sequences with 40 nucleotides(random region). After MAFFT analyses (multiple sequence alignment) we found the top 10 clusters correspond to 26% of the total sequences and good evolution pattern was observed. After motif analyses, we selected 8 sequences for further binding studies. The aptamer library, the primers, NGS indexes used for SELEX experiments and biotinylated aptamer candidates were obtained from Eurogentec, Belgium.

Surface Plasmon Resonance

Surface Plasmon Resonance (SPR) assay was performed to assess the binding affinity of the candidate aptamer sequences to α7/β1 integrin protein. Typically, biotinylated aptamer candidates were immobilized onto the streptavidin chip (CM5) and analysed by Biacore 3000 (GE Healthcare). In this assay, the kinetics rate of the association and dissociation of the aptamer-protein complex and the binding constant were also evaluated. Initially, we immobilised 10 μM of biotinylated aptamers and 3.3 μM of protein was injected. After initial screening of 8 candidates, we performed the saturation studies of the best binding aptamer sequence. Next, we truncated the best candidate sequence, and measured the binding constant of the truncated candidate.

AuNPs synthesis and functionalization

AuNPs were synthesized following the Turkevich method. Briefly, a solution of 945.2 μM hydrogen tetrachloroaurate (III) hydrate in RNAse-free water was stirred and heated at 140 °C under reflux until boiling. Then, a solution of 40 mM sodium citrate tribasic was added, and the mixture was stirred for 15 min. Afterwards, the solution was allowed to reach room temperature and then the as-synthetized AuNPs were first filtered through a 0.3 μm fritted filter, followed by a second filtration through a 0.22 μm PES filter. AuNPs concentration was calculated using the Beer-Lambert law from the value of absorbance at 520 nm, and employing an extinction coefficient of 2.7×10^8 for 13 nm nanoparticles[80].

The different oligonucleotides were purchased from Integrated DNA Technologies (IDT, Coralveille, USA). AuNPs were functionalized with aptamers and different oligonucleotides such as microRNAs (miR-206, miR-39), imaging oligonucleotides (oligodT-cy5). These oligonucleotides were dsRNA or ssDNA, with the passenger strand modified with a thiol group linker (sequences below). A general protocol for the formulation of oligonucleotide-functionalized AuNP is as follows. First, the thiol group from the oligonucleotide is decaged by incubating them with an excess of tris(2-carboxyethyl) phosphine hydrochloride (100 eq) for 2 h at room temperature. Then, the oligonucleotides are added to the AuNP solution, vortexed, and shaken for 20 min. After that, a 5 M NaCl solution is sequentially added every 20-30 min until a final concentration of 0.3 M is reached. Of note, the nanoparticles need to be quickly vortexed after each salt addition to avoid aggregation. Afterward, the nanoparticles are shaken overnight and subsequently centrifuged and washed 3 times with water. The oligonucleotide loading is calculated from the supernatant of the first centrifugation. Finally, the nanoparticles are redispersed in RNA-free water and stored in the fridge until used[37]. AuNPs oligonucleotide loadings were 2 ± 0.1 μM. AuNPs concentration in all groups was adjusted to 33.6 nM and they were filtered with a syringe filter 0.2 μm in a laminar flow hood.

Cargo oligonucleotides sequences

Cargo	Sequence (5′→3′)
miR-206	UGGAAUGUAAGGAAGUGUGUGG
	CCACACACUUCCUUACAUUCCATTTTT thiol
miR-39	UCACCGGGUGUAAAUCAGCUUG
	CAAGCUGAUUUACACCCGGUGATTTTT thiol
oligodT(22)	TTTTTTTTTTTTTTTTTTTTTT thiol
oligodT (37) Cy5	Thiol TTTTTTTTTTTTTTTTTTTTTT TTTTTTTTTTTTTTT Cy5

TEM

AuNPs size and shape were examined by transmission electron microscopy (TEM) in a JEOL JEM 101, operating 100 kV. For that purpose, a drop of AuNPs dilution was placed onto a carbon-coated copper grid and allowed to dry. The size distribution was calculated manually by measuring the mean size of 200 particles with Image J Software[81].

Hydrodynamic size

The hydrodynamic size was measured on a Dynamic Light Scattering (DLS) DLS Zeta Sizer Nano-ZS (Malvern Instruments, UK). For that purpose, AuNPs were diluted to a final concentration of 1 nM in water and the measurements were performed in a standard cuvette for 12 runs of 60 s each 25 °C using a laser at 633 nm.

Z-potential

The Z-potential was measured by DLS Zeta Sizer Nano-ZS (Malvern Instruments). AuNPs were diluted in water solution at 1 nM. NaCl was added until its concentration reached 5 mM. Then, the nanoparticles were measured in a Z-potential cell (Malvern Instruments) at 25 °C. AuNPs displaying a protein corona were prepared following the sucrose cushion step shown below in section **Protein corona**. After that centrifugation step, the nanoparticles were redispersed following the same rationale of the uncoated AuNPs.

Protein corona

The therapeutic candidate containing miR-206 and α7/β1 aptamer was subjected to protein corona studies. For that purpose, a solution of nanoparticles in RNAase-free water (150 μL, $7.73 \cdot 10^{11}$ particles) was incubated with 150 μL of the corresponding plasma at 37 °C for 5 min. Afterwards, the mixture was loaded onto a sucrose cushion (2 × 1 mL, 0.7 M in PBS) and centrifuged (1 h, 18400 g, 4 °C). Then, the supernatant was discarded, and the nanoparticles were collected in one tube using 1.2 mL of PBS and centrifuged again (1 h, 18400 g, 4 °C). This step was carried out twice. Finally, the nanoparticles were dispersed in PBS and stored in the freezer until the different analyses were carried out. The protein corona formed was detached from the surface immediately before the different experiments (SDS-PAGE or mass spectrometry) were carried out to prevent the proteins from adsorbing again onto the gold surface.

For the SDS-PAGE, 25 μL of the corresponding sample were mixed with 25 μL of a solution containing dithiothreitol (200 mM) and sodium docecyl sulfate (100 mM). Then, the samples were placed in a thermoshaker at 90 °C for 10 min. Then, 25 μL of the previously heated solutions were mixed with 25 μL of 2x Laemmli sample buffer and immediately injected into the corresponding well of a 10% polyacrylamide gel. The samples were run at a constant voltage of 140 V, stained with Coomassie blue, and imaged in a Chemidoc Imaging Instrument (Bio-Rad Laboratories).

The mass spectrometry was carried out at the Proteomics Facility of the Spanish National Centre for Biotechnology (CNB), using an Orbitrap Exploris 240 mass spectrometer and the Proteome Discoverer software. The first step was the tryptic digestion. Briefly, the samples ($n = 3$) were diluted with lysis buffer (5% sodium dodecyl sulfate (SDS), 50 mM triethylammonium bicarbonate (TEAB)). Then, samples were reduced and alkylated with 5 mM tris(2-carboxyethyl) phosphine (TCEP) and 10 mM chloroacetamide (CAA) for 30° min at 60 °C. Protein digestion in the S-trap filter (Protifi, Huntington, NY, USA) was carried out according to the manufacturer's instructions with minor modifications[82]. Samples were digested overnight at 37 °C using a protein:trypsin ratio of 15:1, and further cleaned with a StageTip C18 prior to LC-ESI-MS/MS analysis. After desalting the above-mentioned samples, Qubit™ Fluorometric Quantitation (Thermo Fisher Scientific) was employed to determine peptide concentration. Afterwards, 500 ng of the corresponding sample were subjected to 1D-nano LC ESI-MS/MS (Liquid Chromatography Electrospray Ionization Tandem Mass Spectrometric) analysis employing an Ultimate 3000 nano HPLC system (Thermo Fisher Scientific) coupled online to an Orbitrap Exploris 240 mass spectrometer (Thermo Fisher Scientific). The peptides were eluted onto a 50 cm × 75 μm Easy-spray PepMap C18 analytical column at 45 °C and separated at a flow rate of 250 nL/min using a 40 min gradient ranging from 2 % to 95 % mobile phase B (mobile phase A: 0.1% formic acid (FA); mobile phase B: 100 % acetonitrile (ACN), 0.1 % FA). The injection volume was 5 μl and the loading solvent 2 % ACN in 0.1 % FA.

Data acquisition was carried out employing a data-dependent top-20 method, in full scan positive mode, scanning 350 – 1200 m/z. Survey scans were acquired at a resolution of 60,000 at m/z 200, with Normalized Automatic Gain Control (AGC) target (%) of 300 and a maximum injection time (IT) of 40 ms. The top 20 most intense ions from each MS1 scan were selected and fragmented via Higher-energy collisional dissociation (HCD). Resolution for HCD spectra was set to 45,000 at m/z 200, with AGC target of 200 and maximum ion injection time of 120 ms. Isolation of precursors was performed with a window of 1 m/z, exclusion duration (s) of 45 and the HCD collision energy was 32. Precursor ions with single, unassigned, or six and higher charge states from fragmentation selection were discarded. Raw instrument files were processed using Proteome Discoverer (PD) version 2.5.0.400 (Thermo Fisher Scientific). MS2 spectra were searched using Mascot Server v2.8.0 (Matrix Science, London, UK) against a *Mus musculus* UniProtKB database (20190314, 22,356 sequences) containing the most common laboratory contaminants (cRAP database with 70 sequences). All searches were configured with dynamic modifications for pyrrolidone from Q (-17.027 Da) and oxidation of methionine residues (+ 15.9949 Da) and static modification as carbamidomethyl (+ 57.021 Da) on cysteine, monoisotopic masses, and trypsin cleavage (max 2 missed cleavages). The peptide precursor mass tolerance was 10 ppm, and MS/MS tolerance was 0.02 Da. The false discovery rate (FDR) for proteins, peptides, and peptide spectral matches (PSMs) peptides was kept at 1%. Overall, proteins were identified with >1 unique peptides with minor exceptions. Those proteins that did not appear in the three replicates were discarded.

Precursor ion quantitation was carried out in Proteome Discoverer as well, using the "Minora" feature in the processing method and the "Feature Mapper" and "Precursor Ions Quantifier" nodes in the consensus step. Protein abundances were calculated by summing sample abundances of the connected peptide groups (using unique +razor peptides).

Cell lines

C2.C12 (C2C12) cells were obtained from ATTC and cultured in growth medium (GM) (DMEM without pyruvate (#61965-026, Gibco)), supplemented with 10% of FBS (#16000044, Gibco). Cells were incubated with the different AuNPs at the final concentration indicated in each experiment and then collected for cytofluorimetric analysis, confocal microscopy, luciferase reporter and cytotoxicity assays as described below.

Cytotoxicity assay

C2C12 cells were seeded in 96-well plates (10000 cells/well) and treated at 60 % confluency with the indicated AuNPs at different concentrations (0.1, 1, 2.5, 5, 10 and 20 nM) in GM medium. After 24 h of incubation, cells were washed twice with PBS to remove the non-internalized nanoparticles. Then, cell viability was measured 72 h after the treatment using a solution of resazurin sodium salt (1% v/v; Sigma Aldrich) in GM medium to the cells as a reported. After 3 h in the incubator, the fluorescence of the media was measured in a Synergy H4 microplate reader (λex: 550 nm, λem: 590 nm). The fluorescence intensity measurements were processed according to the equation:

$$\%\text{cell viability} = \left(\frac{\text{sample data} - \text{negative control}}{\text{positive control} - \text{negative control}}\right) \times 100$$

Luciferase reporter assay

MiR-206 sequence was cloned in pmirGLO dual luciferase reporter (Promega) according to the manufactured specifications. For that purpose, 100 ng/well miR-206 pmirGLO plasmid were transfected in C2C12 cells using lipofectamine following manufacturer indications. After 4 h, the cells were washed and treated with 1 nM of AuNP miR-206. 24 h later, the cells were lysed, and the kit Dual-luciferase reporter assay system (Promega) was used in a plate reader Synergy H4 (Biotek) according to the manufactured specifications. Results were normalized and represented as percentages.

Animals and in vivo treatments

All experiments in this study were performed in D2.B10-Dmd^{mdx}/J (D2-mdx) mice, provided by Jackson Laboratory (Bar Harbor, ME, USA). Mice were housed in ventilated cages with a 12 h light/dark cycle and free access to water and chow. Eight-weeks old mice of both sexes were used for in vivo experiments and MuSCs isolation. Animals were randomly assigned within the experimental groups. Procedures involving mice were corformed to institutional guidelines that comply with national and international laws and policies (DL 26/2014; EEC Council Directive 2010/63/UE) and they were be approved by the Italian Ministry of Health.

Local administration of AuNPs (20 µl) was performed by intramuscular injection of α7/β1 AuNPs oligodT and α7/β1 AuNPs miR-206 into the TA muscles. Mice were treated once a week for a total of 3 weeks. Oligonucleotides (oligodT/miRNA mimics) were delivered at a concentration of 0,5 mg/kg per injection.

AuNPs systemic delivery was obtained by intravenous injection in the lateral tail vein. Briefly, the injection was performed under anaesthesia by intraperitoneal injection of 40 mg/kg ketamine (Zoletil®) and 10 mg/kg xylazine (Rampum®). For long-term treatments, mice were injected with 50 µl of resuspended AuNPs once a week for a total of three or 5 weeks, depending on the experiment. Oligonucleotides (oligodT/miRNA mimics) were delivered at a concentration of 1.2 mg/kg per injection. For biodistribution experiments, mice were injected with 150 µl of α7/β1 or scramble AuNPs containing oligodT-cy5, oligodT, or miR-39 mimics in the lateral tail vein (final oligonucleotide dose of 1.8 mg/kg). Injection was performed under anaesthesia by intraperitoneal injection of 40 mg/kg ketamine (Zoletil®) and 10 mg/kg xylazine (Rampum®) as above. Mice were sacrificed 24 h after treatment and the different organs were collected to analyse the released fluorescence using an IVIS imaging system (Lumina series III) or to perform flow cytometry, qRT-PCR and ICP-MS analysis.

Forelimb strength was measured once a week using a grip strength meter (Bioseb Bio GS-3). Five measurements for each mouse were recorded, and the average maximal strength (Fmax) was normalized to the mouse body weight in order to calculate the absolute grip strength. The procedure was compliant with the standard operating procedures of the TREAT−NMD Neuromuscular Network.

ICP-MS

Organs from treated mice were dried for 72 h at 140 °C in vials. Then the organs were digested in 1 ml Aqua Regia for 48 h. After that, the dissolutions were diluted up to 10 ml in water and filtered with 0.2 µm syringe filters. The gold concentration was measured by ICP-MS in a iCAP-Q ICP-MS equipment (Thermo Scientific, Bremen, Germany) with an automatic atomic sampler ASX-500 (CETAC Technologies, Omaha, USA) in the mass spectroscopy service of CICbiomaGUNE (San Sebastian, Spain).

Single-fibre isolation and culture

Single fibres were isolated from gastrocnemius and soleus muscles of D2.B10-Dmd^{mdx}/J (mdx) mice by digestion with 0,35% collagenase I (#C0130, Sigma) in DMEM with pyruvate, 4.5 g/l glucose and glutamate (# 31966-021, Gibco) for 1 h at 37 °C. Fibres were then cultured in proliferation medium, GM1: DMEM with pyruvate,4.5 g/l glucose and glutamate (# 31966-021, Gibco), supplemented with 10% horse serum (HS, #26050-070, Gibco) and 0.5% chicken embryo extract (CEE, #CE-650-F, Seralab) and penicillin/streptomycin. Myofibres were then treated with either PBS, α7/β1 AuNPs miR-206 or α7/β1 AuNPs oligodT at a final concentration of 6,7 nM, for 24-48 h. After treatment, the fibres were fixed in 4% paraformaldehyde (PFA) for immunostaining.

FACS isolation and MuSCs culture

Hindlimb muscle were digested in PBS containing Mg and Ca (# 14040133, Gibco) with 2 µg/ml collagenase A (#S10103586001, Roche), 2,4 U/mL dispase I (Roche) and 10 ng/mL DNase I (#10104159001, Roche), for 40 min at 37 °C. Cells were then blocked in HBSS buffer (# 14170-088) containing 10% goat serum for 5 min and isolated based on fluorophore levels using FACS MoFlo Astrios EQ High Speed Cell Sorter (Backman Coulter). The following antibodies were used: CD45-eFluor 450 (1/50, #48-0451-82, leucocyte common antigen, Ly-5, eBioscience), CD31-eFluor 450 (1/50, PECAM-1, #48-0311-82, eBioscience), TER-119-eFluor 450 (1/50, clone TER-119, #48-5921-82, eBioscience), Sca1-FITC (1/50, Ly-6 A/E FITC, clone D7, #11-5981-82, eBioscience), ITGA7-649 (1/500, AbLab #67-0010-01). MuSCs were isolated as TER119 − /CD45 − /CD31 − /ITGA7 + /SCA-1− cells; FAPs were isolated as TER119 − /CD45 − /CD31 − /ITGA7-/SCA-1+ cells; Macrophages were isolated as TER119 + /CD45 + /CD31 + /F480 + / CD11b+ cells.

For ex vivo experiments isolated MuSCs were plated at low density on cell culture dishes coated with gelatin 0,1% (#07903, Stemcell) and cultured in BIO-ANF-2 medium (Biological industries) for 24 h. Then, medium was changed to growth medium, GM2: DMEM with

Pyruvate (#41966, Gibco) supplemented with 20% FBS (#16000044, Gibco), 10% HS (#26050-070, Gibco), 1% CEE (#CE-650-F, Seralab) and 1% penicillin–streptomycin (#15140, Gibco) and cells were incubated with α7/β1 AuNPs miR-206 or α7/β1 AuNPs oligodT at a final concentration of 6.7 nM for 48 h.

RNA extraction and qRT-PCR

Total RNA from either cells or whole muscle was extracted using TRIzol reagent (#T9424, Sigma), following manufacturer indications. 0,5-1 μg were then retro-transcribed using PrimeScript Reagent kit (#RR037A, Takara). The cDNA was used as a template in real-time PCR reactions, performed with TB Green® Premix Ex Taq™ II (Tli RNase H Plus) (#RR82LR Takara). Real-time qPCR was performed using primers (Mm GAPDH FW 5′ GAAGGTCGGTGTGAACGGAT 3′; Mm GAPDH RV 5′ ACTGTGCCGTTGAATTTGCC 3′; Mm Myog FW 5′ GTCCCAACCCAGGAGATCAT 3′; Mm Myog RV 5′ CCACGATGGACGTAAGGGAG 3′; MmMyh2 FW 5′ CACAAGGCATCCTCAAGGACA 3′; Mm Myh2 RV 5′ CAGCATCGGGACAGCCTTAC 3′; Mm U6 FW: 5′ TCTACCGGTTTGG CGGTCC 3′; Mm U6 RV: 5′GCACATAGCGGACGACTGAG 3′).

Real-time qRT-PCR for miR-206 and miR-39 were performed using the following primers: Universal primer: RV CATGATCAGCTGGGCCAAGA (Sigma); LNA oligonucleotide (miR-206), design ID: 666230; LNA oligonucleotide (miR-39), design ID: YCO0210528.

Cytofluorimetry experiments

Fluorescence of C2C12 cells incubated for 24 h with AuNPs-cy5 were revealed using a CytoFLEX flow cytometer (Beckman Coulter) and analysed using the FlowJo software v 10.8.1.

For aptamer staining on muscle-resident cell populations, hindlimb muscle were digested in PBS containing Mg and Ca (# 14040133, Gibco) with 2 μg/ml collagenase A (Roche) and 2,4 U/mL dispase I (Roche), for 40 min at 37 °C. Cells were then blocked in HBSS buffer containing 10% goat serum. To evaluate aptamer specific binding, cells were first blocked with yeast tRNA (1 mg/ml) and stained using followed antibodies: CD45-eFluor 450 (1/50, #48-0451-82, leucocyte common antigen, Ly-5, eBioscience), CD31-eFluor 450 (1/50, PECAM-1, #48-0311-82, eBioscience), TER-119-eFluor 450 (1/50, clone TER-119, #48-5921-82, eBioscience) and Sca1-FITC (1/50, Ly-6 A/E FITC, clone D7, #11-5981-82, eBioscience). In addition, cells were incubated with α7/β1 or scramble aptamers labelled with Alexa fluor 594. Before incubation, a folding step was performed. Briefly, 20 μM of Alexa 594-labelled aptamers (#1000913303-Eurogentec) were denatured for 3 min at 90°C in a solution containing 5 mM magnesium acetate, and then cooled down in ice for 5 min. After folding, cells were incubated with the α7/β1 or scramble aptamers for 1 h at +4 °C. Fluorecence was detected using a CytoFLEX flow cytofluorimeter (Beckman coulter). Results were analysed using the FlowJo software v 10.8.1.

For detection of cy5 on muscle-resident cell populations, hindlimb muscles were digested in PBS containing Mg and Ca (# 14040133, Gibco) with 2 μg/ml collagenase A (Roche) and 2,4 U/mL dispase I (Roche), for 40 min at 37 °C. Cells were then blocked in HBSS buffer containing 10% goat serum and stained using followed antibodies:: CD45-eFluor 450 (1/50, #48-0451-82, leucocyte common antigen, Ly-5, eBioscience), CD31-eFluor 450 (1/50, PECAM-1, #48-0311-82, eBioscience), TER-119-eFluor 450 (1/50, clone TER-119, #48-5921-82, eBioscience), Sca1-FITC (1/50, Ly-6 A/E FITC, clone D7, #11-5981-82, eBioscience), ITGA7-PE (1/50, Miltenyi Biotec, Clone 3C12, #130-120-812). MuSCs were identified as TER119−/CD45−/CD31−/ITGA7+/SCA-1− cells; FAPs were identified as TER119−/CD45−/CD31−/ITGA7-/SCA-1+ cells; Lineage positive cells were identified as TER119+/CD45+/CD31+. Cy5 fluorescence within the indicated populations was detected using a a CytoFLEX flow cytofluorimeter (Beckman coulter). Results were analysed using the FlowJo software v 10.8.1.

Immunofluorescence and aptamer hybridization

Immunofluorescence: Cryosections and cells were fixed in 4% PFA for 10 min at RT and permeabilized with 100% cold acetone (#32201, Sigma) or 100% cold methanol (#32213, Sigma) for 6 min at −20 °C. Muscle sections were blocked for 1 h with a solution containing 4% BSA (#A7030, Sigma) in PBS. For PAX7 staining an antigen retrieval step was performed by incubating the cryosections with 0.01% of hot citric acid, pH 6.0, for 10 min The primary antibody incubation was performed O.N. at 4 °C and then, the antibody binding specificity was revealed using secondary antibodies coupled to Alexa Fluor 488, 594, or 647 (Invitrogen). Sections were incubated with DAPI in PBS for 5 min for nuclear staining, washed in PBS, and mounted with glycerol 3:1 in PBS. The primary antibodies used for immunofluorescences are as follows: rabbit anti-Laminin (1/400, #L9393, Sigma); mouse anti-eMyHC (1/20, #F1.652, Developmental Studies Hybridoma Bank, DSHB, http://dshb.biology.uiowa.edu/F1- 652); mouse anti-MF20 (1:20, Developmental Studies Hybridoma Bank, DSHB, http://dshb.biology.uiowa.edu/MF-20); mouse anti-PAX7 (1/10, Developmental Studies Hybridoma Bank, DSHB, http://dshb.biology.uiowa.edu/PAX7);– anti-F4/80 (BM8, Biolegend); rabbit anti-KI67 (1/500, Abcam 15580); mouse anti-MYOD (1/100, 5,8A-NOVUSBIO); rabbit anti-ITGB1 (#4706, Cell Signalling); rabbit anti-ITGA7(H-40, sc-50431, Santa Cruz). Images were acquired with fluorescent microscope and by four-laser Leica confocal microscopy (Microsystems, Concord, ON, Canada) integrated with image capture system and analytical software.

Aptamer staining. Cryosections and myofibres were fixed in PFA 4% for 15 min at RT. The cryosections were then permeabilized with 100% methanol at − 20 °C for 6 min. Single myofibres were permeabilized in 0,1% Triton-X 100 (#T8787) for 20 min at room temperature. Cryosections and myofibres were blocked for 1 h with a solution containing 4% BSA with addition of 0,15 mg/ml salmon sperm DNA (#AM9680- Thermofisher). Then, a folding step was performed. Briefly, 20 μM of Alexa 594-labelled aptamers (#1000913303-Eurogentec) were denatured for 3 min at 90°C in a solution containing 5 mM magnesium acetate, and then cooled down in ice for 5 min. Finally, cryosections and myofibres were incubated with 100 nM α7/β1 or scramble aptamer for 1 h at +4 °C. Nuclei were counterstained with DAPI. Images were acquired with fluorescent microscope and by four-laser Leica confocal microscopy (Microsystems, Concord, ON, Canada) integrated with image capture system and analytical software.

Histological analysis and in situ hybridization

Sirius red staining was performed to analyse total collagens I and III content. Briefly, muscle cryosections were fixed for an 1 h at 56 °C in Bouin's Solution (#HT10132-Sigma) and then stained in Picrosirius red solution (0.1%) (#09189) for 1 h protected from light. After a brief washing step in acidified water 0.5% v/v, sections were fixed in 100% ethanol (#1009866010-Sigma) and a final dehydration step was performed in xylene 100% (#534056). Sections were mounted with EUKITT® (#05393) and visualized using a Nikon Eclipse 90i.

miRNA in situ *hybridization* was performed in formaldehyde- and carbodiimide (EDC)-fixed TA cryosections (0.16 M 90 min at RT, #25952-53-8, Merck KGaA). After washing with 0.2% glycine (#G8898, Sigma) and TBS, cryosections were acetylated using 0.1 M triethanolamine and 0.25% acetic anhydride for 25 min at RT (respectively, #90275, #A6404, Sigma). These steps were followed by a pre-hybridization using 2× SSC, 25% formamide (#F9037, Sigma), and 0.2% Triton (#X100, Sigma) for 30 min at RT, and by the overnight hybridization at 4 °C with the hsa-miR206 probe (10 pmol, #18100-01, Exiqon) dissolved in a solution of 50% formamide, 250 μg/ml tRNA (#R1753, Sigma), 200 mg/ml ssDNA (#D7656, Sigma), 10% dextran sulphate (#D8906, Sigma), and 2× SSC. The hybridization was followed by specific washes with SSC to eliminate non-specific binding of the probe (5× SSC 5 min at RT, 1× SSC 15 min at 45 °C, 2% BSA in 0.2× SSC 15 min at 4 °C, 2× SSC 5 min at RT, TN buffer 10 min at RT, and TNT buffer 15 min at RT) and by the incubation of cryosection using anti-digoxigenin-ap Fab fragments (1/100, #11093274910, Roche) dissolved in TN buffer for 2 h at RT. To reveal the miRNA probe specific binding, cryosections, covered from light, were incubating overnight at 4 °C with 0.375 mg/ml of NBT and 0.188 mg/ml BCIP dissolved in a solution of TMN buffer (respectively, #11383213001 and #11383221001, Roche). TN buffer is composed of 0.1 M Tris–HCl (#T1503, Sigma) and 0.15 M NaCl (#S3014, Sigma) at pH 7.5; TNT buffer is TN buffer with 0.1% Tween (#P1379, Sigma), while TMN buffer is composed of 0.1 M Tris–HCl, 0.005 M MgCl2 (#M8366, Sigma), 0.5 M NaCl, and 2 mM of Levamisole (#L9756, Sigma).

Silver enhancement was performed using a silver enhancer kit (sigma Aldrich SE100-1KT) following manufacturer indications. Briefly sections were fixed in 2.5% glutaraldehyde solution (#G6257) for 15 min and washed in distilled water to remove all traces of chlorides and buffer salts. The specimen was then covered with a silver enhancer mixture for 15 min a 20 °C. After a washing step, the specimen was fixed in 2,5% sodium thiosulfate for 3 min, washed, and mounted.

Hematoxilin/ Eosin staining was performed to analyse tissue morphology and integrity. Briefly, muscle, liver and spleen cryosection were fixed in PFA 4% for 15 min at RT and then stained with with Mayer's Hematoxylin for 8 min followed by washing in running tap water for 10'. Eosin counterstain was applied for 1' a RT. Following staining, slides were dehydrated through 75%, 90% and absolute alcohol cleared in Xylene and mounted with Eukitt (Sigma Aldrich, 03989).

Necrotic fibres staining was performed as follows. Muscle cryosection were fixed in PFA 4% for 15 min at RT and blocked for 1 h with a solution containing 4% BSA (#A7030, Sigma) in PBS. Then sections were incubated with secondary antibody anti-mouse coupled to Alexa Fluor 594. Finally, sections were incubated with DAPI in PBS for 5 min for nuclear staining, washed in PBS, and mounted with glycerol 3:1 in PBS.

Images were analysed using ImageJ software (https://imagej.nih.gov/ij/download.html). For the analysis of the fibrotic area, an algorithm for colour deconvolution was used.

Statistics and reproducibility

The number of independent biological replicates is reported in the figure legends. Statistical analysis was performed using GraphPadPrism8. Normal distribution was first assessed. Comparisons between groups were made using one way and two way ANOVA followed by Tukey's or Kruskal-Wallis *post hoc* test, as indicated in the figure legends. Significance is defined as: $p < 0.05$ (*/#), $p < 0.01$ (**), $p < 0.001$ (***) and $p < 0.0001$ (****). Sample exclusion was not performed unless statistically significant outliers were identified using Grubb's test (extreme studentized method). The exact *p*-values for all the experiments are provided in the Source Data file.

Ethics

Every experiment involving animals have been carried out following a protocol approved by an ethical commission.

Reporting summary

Further information on research design is available in the Nature Portfolio Reporting Summary linked to this article.

Data availability

The mass spectrometry proteomics data have been deposited to the ProteomeXchange Consortium via the PRIDE[83] partner repository with the dataset identifier PXD049295 and 10.6019/PXD049295 (https://doi.org/10.6019/PXD049295). Specific sequences obtained through the SELEX process are not disclosed here as they are under patent evaluation and are considered confidential information. The material is available upon request, after payment of a cost-recovery fee. All other data supporting the findings of this study are available within the paper and its Supplementary Information. Source data are provided with this paper.

References

1. Mendell, J. R. et al. Evidence-based path to newborn screening for Duchenne muscular dystrophy. *Ann. Neurol.* **71**, 304–313 (2012).
2. Ervasti, J. M. & Sonnemann, K. J. Biology of the striated muscle dystrophin-glycoprotein complex. *Int Rev. Cytol.* **265**, 191–225 (2008).
3. Waldrop, M. A. & Flanigan, K. M. Update in Duchenne and Becker muscular dystrophy. *Curr. Opin. Neurol.* **32**, 722 (2019).
4. Duan, D., Goemans, N., Takeda, S., Mercuri, E. & Aartsma-Rus, A. Duchenne muscular dystrophy. *Nat. Rev. Dis. Prim.* **7**, 1–19 (2021).
5. Chamberlain, J. S. et al. Microdystrophin expression as a surrogate endpoint for Duchenne muscular dystrophy clinical trials. *Hum. Gene Ther.* **34**, 404–415 (2023).
6. Hammond, S. M. et al. Delivery of oligonucleotide-based therapeutics: challenges and opportunities. *EMBO Mol. Med.* **13**, e13243 (2021).
7. Crudele, J. M. & Chamberlain, J. S. AAV-based gene therapies for the muscular dystrophies. *Hum. Mol. Genet* **28**, R102–R107 (2019).
8. Chang, N. C. et al. The Dystrophin glycoprotein complex regulates the epigenetic activation of muscle stem cell commitment. *Cell Stem Cell* **22**, 755–768.e6 (2018).
9. Dumont, N. A. et al. Dystrophin expression in muscle stem cells regulates their polarity and asymmetric division. *Nat. Med.* **21**, 1455–1463 (2015).
10. Kodippili, K. & Rudnicki, M. A. Satellite cell contribution to disease pathology in Duchenne muscular dystrophy. *Front Physiol.* **14**, 1180980 (2023).
11. Wang, Y. X. et al. EGFR-aurka signaling rescues polarity and regeneration defects in dystrophin-deficient muscle stem cells by increasing asymmetric divisions. *Cell Stem Cell* **24**, 419–432.e6 (2019).
12. Sacco, A. et al. Short telomeres and stem cell exhaustion model Duchenne muscular dystrophy in mdx/mTR mice. *Cell* **143**, 1059–1071 (2010).
13. Latella, L. et al. DNA damage signaling mediates the functional antagonism between replicative senescence and terminal muscle differentiation. *Genes Dev.* **31**, 648–659 (2017).
14. Mázala, D. A. et al. TGF-β-driven muscle degeneration and failed regeneration underlie disease onset in a DMD mouse model. *JCI Insight* **5**, e135703 (2020).
15. Mázala, D. A. G. et al. Altered muscle niche contributes to myogenic deficit in the D2-mdx model of severe DMD. *Cell Death Discov.* **9**, 224 (2023).
16. Aránega, A. E. et al. MiRNAs and muscle regeneration: therapeutic targets in Duchenne muscular dystrophy. *Int J. Mol. Sci.* **22**, 4236 (2021).
17. Bartel, D. P. MicroRNAs: target recognition and regulatory functions. *Cell* **136**, 215–233 (2009).
18. Rao, P. K., Kumar, R. M., Farkhondeh, M., Baskerville, S. & Lodish, H. F. Myogenic factors that regulate expression of muscle-specific microRNAs. *Proc. Natl Acad. Sci. USA* **103**, 8721–8726 (2006).
19. Chen, J.-F. et al. The role of microRNA-1 and microRNA-133 in skeletal muscle proliferation and differentiation. *Nat. Genet* **38**, 228–233 (2006).
20. Lozano-Velasco, E. et al. A Pitx2-microRNA pathway modulates cell proliferation in myoblasts and skeletal-muscle satellite cells and promotes their commitment to a myogenic cell fate. *Mol. Cell Biol.* **35**, 2892–2909 (2015).
21. Yin, H. et al. MicroRNA-133 controls brown adipose determination in skeletal muscle satellite cells by targeting Prdm16. *Cell Metab.* **17**, 210–224 (2013).
22. Baghdadi, M. B. et al. Notch-Induced miR-708 antagonizes satellite cell migration and maintains quiescence. *Cell Stem Cell* **23**, 859–868.e5 (2018).

23. Castel, D. et al. Small-RNA sequencing identifies dynamic microRNA deregulation during skeletal muscle lineage progression. *Sci. Rep.* **8**, 4208 (2018).
24. Mytidou, C. et al. Muscle-derived exosomes encapsulate myomiRs and are involved in local skeletal muscle tissue communication. *FASEB J.* **35**, e21279 (2021).
25. Sandonà, M. et al. HDAC inhibitors tune miRNAs in extracellular vesicles of dystrophic muscle-resident mesenchymal cells. *EMBO Rep.* **21**, e50863 (2020).
26. Saccone, V. et al. HDAC-regulated myomiRs control BAF60 variant exchange and direct the functional phenotype of fibro-adipogenic progenitors in dystrophic muscles. *Genes Dev.* **28**, 841–857 (2014).
27. Liu, N. et al. microRNA-206 promotes skeletal muscle regeneration and delays progression of Duchenne muscular dystrophy in mice. *J. Clin. Invest.* **122**, 2054–2065 (2012).
28. Consalvi, S. et al. Preclinical studies in the mdx mouse model of Duchenne muscular dystrophy with the histone deacetylase inhibitor givinostat. *Mol. Med.* **19**, 79–87 (2013).
29. Mozzetta, C. et al. Fibroadipogenic progenitors mediate the ability of HDAC inhibitors to promote regeneration in dystrophic muscles of young, but not old Mdx mice. *EMBO Mol. Med.* **5**, 626–639 (2013).
30. Minetti, G. C. et al. Functional and morphological recovery of dystrophic muscles in mice treated with deacetylase inhibitors. *Nat. Med.* **12**, 1147–1150 (2006).
31. Mercuri, E. et al. Safety and efficacy of givinostat in boys with Duchenne muscular dystrophy (EPIDYS): a multicentre, randomised, double-blind, placebo-controlled, phase 3 trial. *Lancet Neurol.* **23**, 393–403 (2024).
32. Latorre, A. et al. DNA and aptamer stabilized gold nanoparticles for targeted delivery of anticancer therapeutics. *Nanoscale* **6**, 7436–7442 (2014).
33. Zhang, R., Kiessling, F., Lammers, T. & Pallares, R. M. Clinical translation of gold nanoparticles. *Drug Deliv. Transl. Res.* **13**, 378–385 (2023).
34. Xue, H. Y., Liu, S. & Wong, H. L. Nanotoxicity: A key obstacle to clinical translation of siRNA-based. *Nanomed. Nanomed.* **9**, 295–312 (2014).
35. Kouri, F. M. et al. miR-182 integrates apoptosis, growth, and differentiation programs in glioblastoma. *Genes Dev.* **29**, 732–745 (2015).
36. Jensen, S. A. et al. Spherical nucleic acid nanoparticle conjugates as an RNAi-based therapy for glioblastoma. *Sci. Transl. Med.* **5**, 209ra152 (2013).
37. Milán-Rois, P., Rodriguez-Diaz, C., Castellanos, M. & Somoza, Á. Conjugation of nucleic acids and drugs to gold nanoparticles. *Methods Mol. Biol.* **2434**, 103–116 (2022).
38. Cutler, J. I., Auyeung, E. & Mirkin, C. A. *Spherical Nucleic Acids*. Vol. 4 (Jenny Stanford, 2020).
39. Mokhtarzadeh, A. et al. Applications of spherical nucleic acid nanoparticles as delivery systems. *Trends Mol. Med* **25**, 1066–1079 (2019).
40. Burkin, D. J. et al. Transgenic expression of {alpha}7{beta}1 integrin maintains muscle integrity, increases regenerative capacity, promotes hypertrophy, and reduces cardiomyopathy in dystrophic mice. *Am. J. Pathol.* **166**, 253–263 (2005).
41. Burkin, D. J., Wallace, G. Q., Nicol, K. J., Kaufman, D. J. & Kaufman, S. J. Enhanced expression of the alpha 7 beta 1 integrin reduces muscular dystrophy and restores viability in dystrophic mice. *J. Cell Biol.* **152**, 1207–1218 (2001).
42. Ferreira, D. et al. Gold nanoparticles for vectorization of nucleic acids for cancer therapeutics. *Molecules* **25**, 3489 (2020).
43. Kanu, G. A., Parambath, J. B. M., Abu Odeh, R. O. & Mohamed, A. A. Gold nanoparticle-mediated gene therapy. *Cancers* **14**, 5366 (2022).
44. Wang, W., Wang, J. & Ding, Y. Gold nanoparticle-conjugated nanomedicine: design, construction, and structure–efficacy relationship studies. *J. Mater. Chem. B* **8**, 4813–4830 (2020).
45. Fellows, T. et al. Gold nanoparticle-streptavidin conjugates for rapid and efficient screening of aptamer function in lateral flow sensors using novel CD4-binding aptamers identified through Crossover-SELEX. *Analyst* **145**, 5180–5193 (2020).
46. Vachon, P. H. et al. Integrins (alpha7beta1) in muscle function and survival. Disrupted expression in merosin-deficient congenital muscular dystrophy. *J. Clin. Invest.* **100**, 1870–1881 (1997).
47. Sarathy, A. et al. SU9516 increases α7β1 integrin and ameliorates disease progression in the mdx mouse model of Duchenne muscular dystrophy. *Mol. Ther.* **25**, 1395–1407 (2017).
48. Mitchell, M. J. et al. Engineering precision nanoparticles for drug delivery. *Nat. Rev. Drug Discov.* **20**, 101–124 (2021).
49. Millozzi, F., Papait, A., Bouché, M., Parolini, O. & Palacios, D. Nano-immunomodulation: a new strategy for skeletal muscle diseases and aging? *Int J. Mol. Sci.* **24**, 1175 (2023).
50. Tenzer, S. et al. rapid formation of plasma protein corona critically affects nanoparticle pathophysiology. *Nat. Nanotech.* **8**, 772–781 (2013).
51. Vu, V. P. et al. Immunoglobulin deposition on biomolecule corona determines complement opsonisation efficiency of preclinical and clinical nanoparticles. *Nat. Nanotechnol.* **14**, 260–268 (2019).
52. Ge, J. et al. Gold and gold-silver alloy nanoparticles enhance the myogenic differentiation of myoblasts through p38 MAPK signaling pathway and promote in vivo skeletal muscle regeneration. *Biomaterials* **175**, 19–29 (2018).
53. Colapicchioni, V., Millozzi, F., Parolini, O. & Palacios, D. Nanomedicine, a valuable tool for skeletal muscle disorders: Challenges, promises, and limitations. *Wiley Interdiscip. Rev. Nanomed. Nanobiotechnol.* **14**, e1777 (2022).
54. Brancaccio, A. & Palacios, D. Chromatin signaling in muscle stem cells: interpreting the regenerative microenvironment. *Front. Aging Neurosci.* **7**, 36 (2015).
55. Chen, J.-F. et al. microRNA-1 and microRNA-206 regulate skeletal muscle satellite cell proliferation and differentiation by repressing Pax7. *J. Cell Biol.* **190**, 867–879 (2010).
56. Cutler, A. A. et al. The regenerating skeletal muscle niche drives satellite cell return to quiescence. *iScience* **25**, 104444 (2022).
57. Geary, R. S., Norris, D., Yu, R. & Bennett, C. F. Pharmacokinetics, biodistribution and cell uptake of antisense oligonucleotides. *Adv. Drug Deliv. Rev.* **87**, 46–51 (2015).
58. Du, B. et al. Tailoring kidney transport of organic dyes with low-molecular-weight PEGylation. *Bioconjugate Chem.* **31**, 241–247 (2020).
59. Katoozi, D., Clayton, A. H. A., Moss, D. J. & Chon, J. W. M. Uptake quantification of gold nanoparticles inside of cancer cells using high order image correlation spectroscopy. *Biomed. Opt. Express* **12**, 539–552 (2021).
60. Roberts, T. C., Langer, R. & Wood, M. J. A. Advances in oligonucleotide drug delivery. *Nat. Rev. Drug Discov.* **19**, 673–694 (2020).
61. Hicks, M. R. et al. Nanoparticles systemically biodistribute to regenerating skeletal muscle in DMD. *J. Nanobiotechnol.* **21**, 303 (2023).
62. Rothdiener, M., Beuttler, J., Messerschmidt, S. K. E. & Kontermann, R. E. Antibody targeting of nanoparticles to tumor-specific receptors: immunoliposomes. *Methods Mol. Biol.* **624**, 295–308 (2010).
63. Wang, C.-H. et al. Aptamer-conjugated and drug-loaded acoustic droplets for ultrasound theranosis. *Biomaterials* **33**, 1939–1947 (2012).
64. Acharya, S. & Hill, R. A. High efficacy gold-KDEL peptide-siRNA nanoconstruct-mediated transfection in C2C12 myoblasts and myotubes. *Nanomedicine* **10**, 329–337 (2014).

65. Jativa, S. D. et al. Enhanced delivery of plasmid DNA to skeletal muscle cells using a DLC8-binding peptide and ASSLNIA-modified PAMAM dendrimer. *Mol. Pharm.* **16**, 2376–2384 (2019).
66. Ungerleider, J. L., Kammeyer, J. K., Braden, R. L., Christman, K. L. & Gianneschi, N. C. Enzyme-targeted nanoparticles for delivery to ischemic skeletal muscle. *Polym. Chem.* **8**, 5212–5219 (2017).
67. Malecova, B. et al. Targeted tissue delivery of RNA therapeutics using antibody-oligonucleotide conjugates (AOCs). *Nucleic Acids Res.* **51**, 5901–5910 (2023).
68. Hindi, S. M. et al. Enveloped viruses pseudotyped with mammalian myogenic cell fusogens target skeletal muscle for gene delivery. *Cell* **186**, 2062–2077.e17 (2023).
69. Zhou, G. et al. Aptamers: A promising chemical antibody for cancer therapy. *Oncotarget* **7**, 13446–13463 (2016).
70. Philippou, S. et al. Selection and identification of skeletal-muscle-targeted RNA aptamers. *Mol. Ther. Nucleic Acids* **10**, 199–214 (2018).
71. Fry, C. S., Kirby, T. J., Kosmac, K., McCarthy, J. J. & Peterson, C. A. Myogenic progenitor cells control extracellular matrix production by fibroblasts during skeletal muscle hypertrophy. *Cell Stem Cell* **20**, 56–69 (2017).
72. Latorre, A. & Somoza, Á. Glutathione-triggered drug release from nanostructures. *Curr. Top. Med Chem.* **14**, 2662–2671 (2014).
73. Lushchak, V. I. Glutathione homeostasis and functions: potential targets for medical interventions. *J. Amino Acids* **2012**, 736837 (2012).
74. Meister, A. Glutathione metabolism and its selective modification. *J. Biol. Chem.* **263**, 17205–17208 (1988).
75. Sen, C. K. Glutathione: A key role in skeletal muscle metabolism. In *Oxidative Stress in Skeletal Muscle* (eds. Reznick, A. Z., Packer, L., Sen, C. K., Holloszy, J. O. & Jackson, M. J.) 127–139 (Birkhäuser, Basel, 1998).
76. Hurst, S. J., Lytton-Jean, A. K. R. & Mirkin, C. A. Maximizing DNA loading on a range of gold nanoparticle sizes. *Anal. Chem.* **78**, 8313–8318 (2006).
77. Milan, J., Niemczyk, K. & Kus-Liśkiewicz, M. Treasure on the earth-gold nanoparticles and their biomedical applications. *Materials* **15**, 3355 (2022).
78. Sibuyi, N. R. S. et al. Multifunctional gold nanoparticles for improved diagnostic and therapeutic applications: a review. *Nanoscale Res Lett.* **16**, 174 (2021).
79. Lee, K. et al. Nanoparticle delivery of Cas9 ribonucleoprotein and donor DNA in vivo induces homology-directed DNA repair. *Nat. Biomed. Eng.* **1**, 889–901 (2017).
80. Prigodich, A. E. et al. Nano-flares for mRNA regulation and detection. *ACS Nano* **3**, 2147–2152 (2009).
81. Milán Rois, P., Latorre, A., Rodriguez Diaz, C., Del Moral, Á. & Somoza, Á. Reprogramming cells for synergistic combination therapy with nanotherapeutics against uveal melanoma. *Biomim. (Basel)* **3**, E28 (2018).
82. Ciordia, S. et al. Digging deeper into bile proteome. *J. Proteom.* **230**, 103984 (2021).
83. Perez-Riverol, Y. et al. The PRIDE database resources in 2022: a hub for mass spectrometry-based proteomics evidences. *Nucleic Acids Res.* **50**, D543–D552 (2022).

Acknowledgements

This work was funded by the Eranet-Euronanomed Joint Call 2016 (H2020), project #ER-2016-2360733 to D.P, A.S., and J-J. T and the French Association Against Myopathies, Ignition project #23592 to D.P and A.S. Also, it was partially supported by the Spanish Ministry of Economy and Competitiveness [PID2020-119352RB-I00, PID2023-146982OB-I00], Comunidad de Madrid [S2022/BMD-7403 RENIM-CM], Asociación Española Contra el Cáncer (PRYCO223002PEIN), and IMDEA Nanociencia. F.M. acknowledges a PhD fellowship from Università Sapienza, G.D.C. acknowledges a PhD fellowship from Università Cattolica del Sacro Cuore. M.M. acknowledges support from Ministerio de Ciencia e Innovación (FJC2021-048151-I). I.P. acknowledges a PhD fellowship from the Community of Madrid (Grant No: PIPF-2022SAL-GL-24788). IMDEA Nanociencia receives support from the 'Severo Ochoa' Programme for Centres of Excellence in R&D (MICINN Grant no: CEX2020-001039-S). The authors would like to thank Dr. Pier Lorenzo Puri for critical discussions and helpful suggestions.

Author contributions

D.P., A.So., and J.-J.T. conceived and designed the study. F.M. performed all the in vitro and in vivo experiments and analysed the data with help from G.D.C., M.S., F.E., and M.T.V. P.M.-R. designed and synthetized the nanoparticles, with help from C.R., M.M., and I.P. A.S. performed the SELEX experiments and characterization studies of selected aptamers. M.D.B. performd the cytofluorimetry and FACS analysis. M.G.-G. performed the protein corona experiments. M.B., O.P., and V.S. contributed to data analysis and interpretation. D.P. and A.So. wrote the manuscript with input from J.-J.T., F.M., P.M.-R., A.S. and M.G.-G. All the authors reviewed and approved the manuscript.

Competing interests

A patent application has been filed by the Università Cattolica del Sacro Cuore, IMDEA Nanociencias, Inserm and IRCCS Fondazione Santa Lucia with D.P. A.So., J.-J.T., F.M., P.M.-R and A.S. as inventors (Nucleic acid aptamers recognizing the extra cellular domain of alpha7/beta1 integrin dimers and uses thereof. Application number: 102024000007594.). The other authors declare no competing interests.

Additional information

Supplementary information The online version contains supplementary material available at https://doi.org/10.1038/s41467-024-55223-9.

Correspondence and requests for materials should be addressed to Jean-Jacques Toulmé, Álvaro Somoza or Daniela Palacios.

Peer review information *Nature Communications* thanks the anonymous reviewers for their contribution to the peer review of this work. A peer review file is available.